

DETECTION OF FLUVIAL LANDFORMS UNDERNEATH FORESTS USING LIDAR
DATA

By

HYUN-CHONG CHO

A DISSERTATION PRESENTED TO THE GRADUATE SCHOOL
OF THE UNIVERSITY OF FLORIDA IN PARTIAL FULFILLMENT
OF THE REQUIREMENTS FOR THE DEGREE OF
DOCTOR OF PHILOSOPHY

UNIVERSITY OF FLORIDA

2009

© 2009 Hyun-chong Cho

To my father, mother, sister and brother

ACKNOWLEDGMENTS

First of all, I would like to express the deepest gratitude to my advisor, Dr. K. Clint Slatton. I have been amazingly fortunate to have an advisor who gave me the freedom to explore on my own and at the same time the guidance to recover when my steps faltered. He taught me how to question thoughts and express ideas. His patience and support helped me overcome many crisis situations and finish this dissertation. I hope one day to become as good an advisor to my students as he has been to me. I am also grateful to Dr. Ramesh Shrestha, Dr. Fred J. Taylor, and Dr. John G. Harris for their valuable time and interest in serving on my supervisory committee, as well as their comments, which helped improve the quality of this dissertation.

I have been very fortunate to work with many outstanding graduate students in the Adaptive Signal Processing Laboratory (ASPL). My special acknowledgement goes to Sweungwon Cheung, Pravesh Kumari, Heezin Lee, Carolyn Krekeler, Kristofer Shrestha, Michael Starek, Kittipat Kampa, Abhinav Singhanian, Bidhyananda Yadav, Hojin Jhee, John Caceres, Juan Carlos, Karthik Nagarajan, Kuei-Tsung Shih, Michael Sartori, Pang-wei Liu, Raghavendra Kumar, Thelma Epperson, Tory Cobb, and Tristan Cossio for their help, collaboration and valuable discussions. They also brought me continuous fun, which was essential during my PhD study. I owe much to them all.

Finally, my utmost appreciation goes to my sister and brother for always believing in me. Their unceasing love and whole-hearted support made finishing this work possible. Last but not most, I thank my parents, for their love, support, patience, and late-night prayers.

TABLE OF CONTENTS

	<u>page</u>
ACKNOWLEDGMENTS	4
LIST OF TABLES	6
LIST OF FIGURES	7
CHAPTER	
1 INTRODUCTION	11
1.1 Background	11
1.2 Measurement	15
1.3 Site Description	16
2 STREAM CHANNEL DETECTION USING MATHEMATICAL MORPHOLOGY	20
2.1 C-Star Algorithm	20
2.1.1 Basic Algorithm	20
2.1.2 Connecting Stream Segments	22
2.2 Filter Parameter Selection using Simulated Terrain	25
2.2.1 Simulated Data	25
2.2.2 Error Metrics	26
2.3 Simulation and Real Data Result	27
2.3.1 Simulated Data Result	27
2.3.2 Stream Channels Detection in Real Data	28
2.3.3 Features of Stream Channels	30
3 STREAM AND ROAD DETECTION USING DIFFERENTIAL MORPHOLOGICAL PROFILES	50
3.1 Background of Differential Morphological Profiles	50
3.2 Differential Morphological Profiles	52
3.3 Principal Component Analysis	54
3.4 Linear Discriminant Analysis	55
3.5 Bayesian Classification	58
3.6 Result and Discussion	60
3.7 Comparison of C* Algorithm, DMP, and D8	62
4 CONCLUSION AND FUTURE WORK	75
LIST OF REFERENCES	78
BIOGRAPHICAL SKETCH	82

LIST OF TABLES

<u>Table</u>	<u>page</u>
2-1. Error metrics vs. sizes of disk shape SE for simulated data	49
2-2. Error metrics vs. shapes for the “best” size of 7×7 for simulated data	49
3-1. Information classes, training, and test samples for Hogtown Creek site.....	73
3-2. Test accuracies in percentages with variances for Hogtown Creek site.....	73
3-3. Information classes, training, and test samples for Hatchett Creek.....	73
3-4. Test accuracies in percentage with variances for Hatchett Creek	73
3-5. Information classes, training, and test samples for Red Wall Canyon	73
3-6. Test accuracies in percentage with variances for Red Wall Canyon.....	74
3-7. Error metrics vs. all methods on simulation.....	74
3-8. Error metrics vs. all methods on Hogtown Creek	74
3-9. Error metrics vs. all methods on Hatchett Creek.....	74
3-10. Error metrics vs. all methods on Red Wall Canyon	74

LIST OF FIGURES

<u>Figure</u>	<u>page</u>
1-1. Bare-surface DEM _{G3} and DEM _{DS} of Hogtown Creek	18
1-2. Hogtown Creek and Hatchett Creek	19
2-1. A 7×7 disk-shaped binary structuring element.....	36
2-2. Hogtown Creek DEMs of each process in C* algorithm	36
2-3. The 3x3 pixel neighborhood used in the eight-connectivity algorithm.....	37
2-4. Minimum-cost path extraction process for a 3 x 3 image	37
2-5. The connection results of DEM _{DS} over the Hogtown site.....	38
2-6. Simulated DEM of a 200m×1000m ALSM image.....	38
2-7. Definitions of detection errors.....	39
2-8. Testing algorithm on simulated terrain.....	39
2-9. Testing algorithm on another simulated terrain.....	40
2-10. Planform channel detection results at the Hogtown Creek.....	41
2-11. Detection result of C-star algorithm at the Hatchett Creek	42
2-12. Detection result of C-star algorithm at the Red Wall Canyon, Death Valley	43
2-13. Stream channel cross-sections	44
2-14. Cross-sections of survey result, DEM _{G3} and DEM _{DS}	45
2-15. Results of ROC, bank slope asymmetry and tree density in DEM _{G3}	46
2-16. 1-D plots of Hogtown Creek features.....	47
2-17. 2-D figures of Hogtown Creek features.	48
3-1. Morphological Profile for the Hogtown Creek site.....	67
3-2. Example of a DMP for a pixel on a stream in the Hogtown DEM.....	67
3-3. Ground truth over the Hogtown site	68
3-4. Ground truth of Hatchett: Stream (blue), Outside Stream (red).....	68

3-5. Ground truth of Red Wall Canyon: Stream (blue), Outside Stream (red).....	69
3-6. Detection results on simulated data.....	69
3-7. Detection results on Hogtown Creek.....	70
3-8. Detection results on Hatchett Creek.....	71
3-9. Detection results on Red Wall Canyon.....	72

Abstract of Dissertation Presented to the Graduate School
of the University of Florida in Partial Fulfillment of the
Requirements for the Degree of Doctor of Philosophy

DETECTION OF FLUVIAL LANDFORMS UNDERNEATH FORESTS USING LIDAR
DATA

By
Hyun-chong Cho

May 2009

Chair: K. Clint Slatton

Major: Electrical and Computer Engineering

Airborne Laser Swath Mapping (ALSM) instrument technology and subsequent algorithm advances have made it possible over the last several years to map the earth's surface and landcover at unprecedented resolution. The ability of ALSM technology to densely sample ground elevations beneath forest canopies is particularly important because forested watersheds have traditionally been difficult to study with remote sensing techniques. Extraction of stream networks from digital elevation models (DEMs) plays a fundamental role in modeling local and spatially distributed hydrological processes. To detect stream channels, we have developed two approaches. The first approach is based on an encoding of mathematical morphological operators and is shown to systematically and accurately extract stream channel locations, forms, and incipient incisions in a forested watershed. The accuracy of the method is verified using a set of error measures over simulated terrain and also over real terrain where the site was manually surveyed. The second approach represents an alternative to the first, and it consists of three steps. First, the composition of geodesic tophat and bothat operations of different sizes is used in order to build a differential morphological profile that records image structural information. The use of morphological operations at multiple scales can capture a wider variety of surface forms, but it also leads to a high-dimensional parameter space that often contains redundant information.

Therefore, in the second step, feature selection is investigated using both Principal Component Analysis (PCA) and Linear Discriminant Analysis (LDA). Third, a Bayesian classification is used to classify the features resulting from the second step. In experiments, the two proposed methods perform well in terms of detection results and classification accuracies. The second approach is more general than the first, but also requires training and more computation. It will be shown that the second method is better suited for analyzing complex watersheds that contain numerous channels or other surface forms at multiple scales.

CHAPTER 1 INTRODUCTION

1.1 Background

Accurate stream channel delineation is vital for understanding the flow of water over terrain and flood mitigation. Extracting accurate representations of streams from Digital Elevation Models (DEMs) is often a required step in predicting the effects of flowing water on surficial processes such as erosion, sediment transport and shallow landslides, and thus facilitates better decision making and planning in water resource management (Knighton, 1998).

Similar to our stream channel extraction application, some researchers have used LiDAR data to extract different kinds of channel networks. Those applications include the recognition of channel-bed morphology (Cavalli *et al.*, 2007), mapping gully and rill channels (James *et al.*, 2007), exploiting topographic signatures (Lashermes *et al.*, 2007), mapping tidal zone areas (Mason *et al.*, 2006), mapping geomorphological units in mountain areas (Asselen *et al.*, 2006), and mapping river valley environments (Jones *et al.*, 2007), for example.

In the recognition of channel-bed morphology, Cavalli *et al.* (2007) used indicators of the local variability of elevation and slope to distinguish step-pool and riffle-pool reaches, which are continuous parts of streams between two specified points. A heuristic approach was employed using indexes of surface roughness to classify the different morphological units (land forms). Reliance on surface roughness, however, will not generally succeed when extracting small streams (e.g. 2-5 m across) under forest canopy. This is because a non-trivial fraction of LiDAR returns can come from shrubs and the lower parts of tree trunks, thereby modulating the estimated “surface” roughness.

The ability of LiDAR data to map gullies and rill channels in a forested landscape, as investigated in James *et al.* (2007), could potentially improve channel-network maps and

topological models. At the gully reach scale (i.e. 2 m), their attempts to use LiDAR data to extract gully cross-section shapes under forest canopy were less successful due to systematic underestimation of gully depths and overestimation of gully top widths. Limited morphologic accuracy of the data set at this scale may be due to low bare-Earth LiDAR point densities, shadowing of gully bottoms, and filtering of topographic discontinuities during post-processing.

In an effort to exploit topographic signatures, Lashermes *et al.* (2007) showed that certain useful features can be found only when using high resolution (i.e. about 2.6 m average bare earth data spacing, gridded to 1 m) topography, such as that derived from LiDAR. They were able to reveal topographic transitional areas of weak convergence, such as the transitions between hillslopes and valleys. They used wavelet analysis to locally filter elevation data and to detect thresholds in topographic curvature and slope-direction change for defining valleys and probable channelized portions of the valley. This method, however, is only suitable for landforms that are significantly larger than the small stream channels we are interested in detecting.

Mason *et al.* (2006) mapped tidal zone areas based on data from two study sites: River Ems, Germany and Venice Lagoon, Italy. It is seen to give reasonably good results in areas which are not significantly complicated. The algorithm for channel extraction from fused LiDAR and spectral data did not reduce the total error substantially from that using LiDAR data alone due to the higher signal-to-noise ratio present in the LiDAR data compared to that in the spectral data.

Asselen *et al.* (2006) concluded that high-resolution topographical data derived from laser Digital Terrain Models (DTMs) are useful for extracting geomorphological units (e.g. deep incised channel, shallow incised channel and fluvial terrace) in mountainous areas. The geomorphological units extracted from laser elevation data not only represent homogeneous

surface characteristics but can also indicate similar material and genesis (land formation process), but only once interpreted by a geomorphological expert.

In mapping river valley environments, Jones *et al.* (2007) found that sometimes unfiltered LiDAR data, including vegetation and buildings, are more suitable for geomorphological mapping than data that have been filtered to remove these features. This approach relied heavily on visual interpretation, and they found that using derivatives of the original LiDAR data, such as grids of slope gradient or aspect, did not always significantly improve the results of mapping the survey area of interest. This approach, however, is totally inappropriate for heavily forested regions, such as ours, because 85% of the LiDAR returns come from the canopy, and the bare ground is completely obscured in the unfiltered LiDAR data.

The above proposed methods make contributions to several application fields for geomorphological mapping, but they do not focus on extraction of small scale (e.g. 2-5 m across) stream channels under heavy forest canopy. Our proposed approach is a new method to automatically and accurately extract stream channel locations, forms, and incipient incisions in forested watersheds.

Another important issue is the accuracy and sensitivity of LiDAR data extraction, which was examined in (Bowen *et al.*, 2002) and (Lindsay, 2006), respectively. Elevation errors based on measurements over all terrain types are largely attributable to horizontal positioning limitations in areas with variable terrain and large topographic relief. Those indicating cross-sectional profile algorithms that were effective for removing vegetation in relatively flat terrain were less effective near the active channel where dense vegetation was found in a narrow band along a low terrace. Accuracy of LiDAR elevation data varies depending on terrain type. Most published estimates of LiDAR accuracy reflect values obtained in relatively flat, homogeneous

terrain. Although LiDAR is capable of producing 15 to 20 cm RMSE (z) elevation data, horizontal positioning limitations (1 to 2 m RMSE (x, y)) associated with each laser return increase the probability of larger observed elevation errors in areas with variable terrain and large topographic relief. LiDAR elevation data are based on systematic random sampling by a scanning laser. This limits the user's ability to define linear features, such as the top of a steep bank, at a resolution smaller than the distance between sample points, which can be as large as 1 to 5 m in many LiDAR data sets (Bowen *et al.*, 2002).

A series of stochastic simulations was used to evaluate the sensitivity of DEM based channel mapping techniques to the magnitude and spatial autocorrelation of elevation error, even before the advent of high resolution LiDAR data. Those automated channel extraction techniques that utilize digital terrain data can be categorized as valley recognition (VR) methods, channel initiation (CI) methods, or combinations of the two. The channel-mapping algorithms in (Lindsay, 2006), (Douglas, 1986), (Johnston *et al.*, 1975), and (Peucker *et al.*, 1975) are based on identifying patterns in surface morphology and are particularly susceptible to errors resulting from surface roughness. Algorithms in (O'Callaghan *et al.*, 1984), and (Montgomery *et al.*, 1993) are based on simulating overland flow and are also hindered by the greater number of surface depressions occurring on rough surfaces. Although LiDAR data were found to provide a sufficient resolution for mapping fine-scale headwater channels, the greater surface roughness did present challenges for automated channel-mapping techniques (Lindsay, 2006).

River system analysis has traditionally been limited to conventional ground surveys and repeated field measurements. Advances in the mapping and remote sensing technology gradually led to the advent of using aerial photography, digital imagery, and radar data for the delineation of streams. Laliberte *et al.* (2001) used aerial photographs of different time periods

to compare the changes in channel outlines and stream widths over a yearly period. The task of identifying the stream boundaries in planform was generally limited to manual digitization of imagery, and in most cases, three-dimensional (3D) stream cross-section measurements still had to be collected through field observations, unless inferred from stereo optical or interferometric radar methods, each of which has significant 3D resolution limitations at meter scales.

Furthermore, neither passive optical nor radar techniques could accurately detect streams covered over by dense forest canopy. Thus, the study of fluvial and erosional processes in many forested watersheds remains problematic. Airborne Laser Swath Mapping (ALSM), also known as LiDAR, with its high 3D spatial resolution and vegetation penetration capability, offers a powerful new technology that can be applied to this problem. However, the ALSM data must be combined with specialized algorithms to systematically extract the channels.

1.2 Measurement

Before 2007, National Center for Airborne Laser Mapping (NCALM) operated an Optech 1233 model ALSM system. It was capable of a 33 kHz laser pulse rate, recorded two returns (first and last) per laser shot, and had a fixed beam divergence of 0.25 milliradians. In February 2007, NCALM took delivery of and has since calibrated a new generation of ALSM instrument (Shrestha *et al.*, 2007). The Optech Gemini model is capable of laser pulse rates up to 167 kHz, records four returns (including first and last) per shot, and has a switchable beam divergence of 0.25 mrad and 0.80 mrad.

Early testing of the Gemini unit by NCALM revealed an upward trend in elevation error rms with increasing laser pulse rate (Shrestha *et al.*, 2007). Furthermore, it was desired to characterize the bare-surface sampling capability of the Gemini system at different pulse rates and beam divergences. In a series of experiments, the Gemini was operated at different settings for three repeat passes of a forested test site. The laser pulse rate and beam divergence settings

for the three flights were (1st) 142 kHz and 0.25 mrad, (2nd) 125 kHz and 0.25 mrad, (3rd) 125 kHz and 0.80 mrad. The Above Ground Level (AGL) flying altitude was 600 m in all cases. The average spot spacing at ground level was between 40 – 50 cm for each flight, resulting in almost 30 points per square meter when the point clouds from the three flights were merged. However, vegetation filtering tests revealed that only about 17% of the laser shots resulted in returns from the ground, yielding about 5 actual ground points per square meter in the forest.

While valuable for algorithm validation, the DEM that results from this high grade data set (DEM_{G3}) is not necessarily representative of other ALSM-derived DEMs to which researchers might have access (e.g. pre-2007 NCALM data sets). In order to generate a rigorous estimation of what might be possible with a more typical ALSM acquisition, the data files from the two narrow-beam flights were downsampled via the time stamps on each shot to mimic a two-pass acquisition with a laser pulse rate of 33 kHz. A two-pass scenario was assumed since NCALM normally flies all parallel lines with 50% overlap, thus yielding double coverage except on the two bounding flight lines. The downsampled data were filtered to produce a bare-earth DEM (Kampa *et al.*, 2004), which we will refer to as DEM_{DS}. Figure 1-1 shows the bare-surface of DEM_{G3} and DEM_{DS} at Hogtown Creek in Florida, USA. DEM_{G3} has less noise and clearer stream views.

1.3 Site Description

Two forested watersheds (Hogtown Creek and Hatchett Creek) located within roughly 10km of each other in North-Central Florida, USA and the deformed landforms along the northern Death Valley fault zone (i.e. Red Wall Canyon) are examined. The Hogtown Creek Watershed drains 20 square miles of mostly urban and suburban development along with some greenbelt while the Hatchett Creek Watershed drains nearly 65 sq. mi. of rural forests. Both watersheds have low topographic relief on the order of 10m overall. The portions of Hogtown

examined here are heavily forested floodplain located in a greenbelt with mixed southern pine and hardwoods, and significant saw palmetto (*Serenoa repens*) understory. The bottomland soils are generally sandy, but range in sand and organic content. Hogtown Creek ALSM data was acquired by Gemini model in March 2007 and Hatchett Creek ALSM data was collected by Optech 1233 model in February 2007, at which time the trees had undergone significant budding, but were far from maximum leaf-out. Figure 1-2 shows pictures of Hogtown Creek and Hatchett Creek.

Red Wall Canyon ALSM data is collected for the study on the northern Death Valley and Fish Lake Valley fault zones, the largest fault system in the region, extending over 300 km from the Garlock fault in the Mojave Desert northward into southwestern Nevada. NCALM (National Center for Airborne Laser Mapping) acquired approximately 2 km × 10 km of LiDAR data at sites centered on 36.87°N/117.26°W and 37.09°N/117.47°W in northern Death Valley, California in February 2005. It is available on the Web [<http://calm.geo.berkeley.edu/ncalm/ddc.html>].

The paper is organized as follows. In Chapter 2, we describe the basic characteristics of a stream channel detection algorithm, which is our first approach, and discuss the experimental results. For validating the approach used in this work, the filter parameter selection using simulated terrain is also discussed. In Chapter 3, we explain the Differential Morphological Profile (DMP) method used to extract streams and roads. To reduce the dimension of DMP, Principal Component Analysis (PCA) and Linear Discriminant Analysis (LDA) are applied. The experimental results of this second approach will also be presented and analyzed. In Chapter 4, the conclusions and future work are described, respectively.

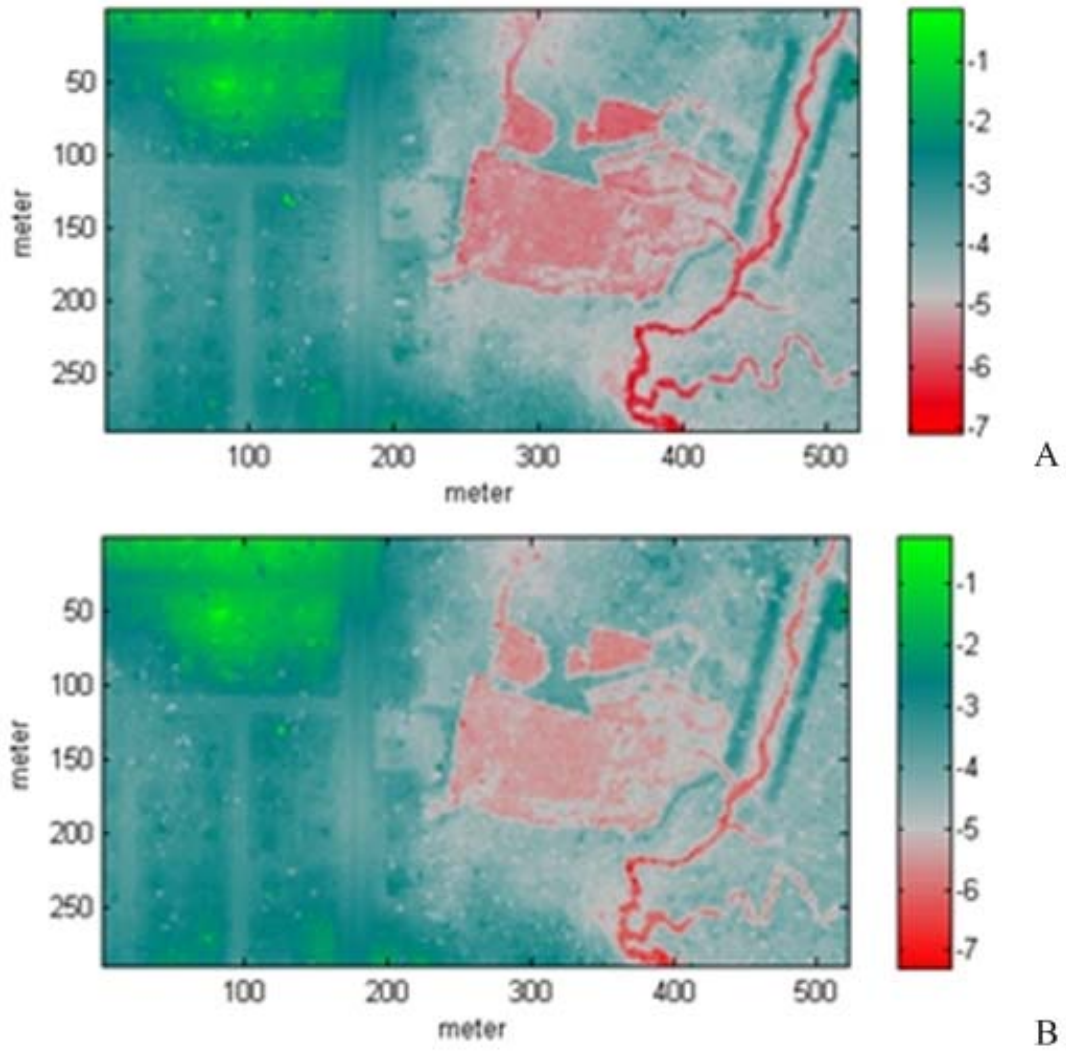


Figure 1-1. Bare-surface DEM_{G3} (A) and DEM_{DS} (B) derived from filtered ALSM data of the Hogtown study site near Gainesville, FL. The imaged area is oriented with North pointing up along the y-axis, and covers an area of 290m×521m with 1m×1m pixels. Total elevation range is 7 meters.

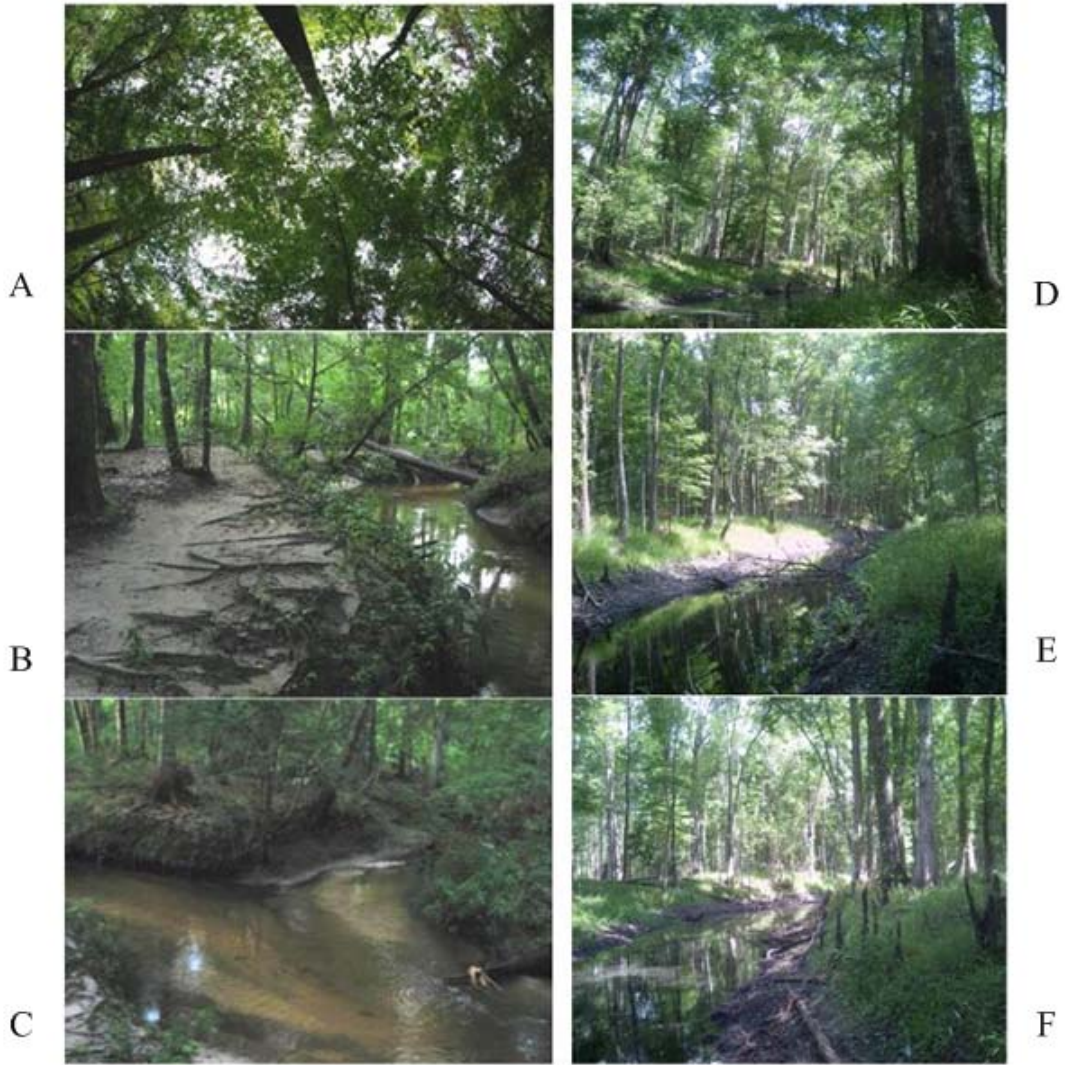


Figure 1-2. Hogtown Creek (A, B, and C) and Hatchett Creek (D, E, and F). They have about 35m tall forest with dense understory. (Irregular tree spacing and structure and uneven-aged: multiple layers of undergrowth and canopy). Channel width at water level is 2-3 m and channel depth is about 10-20 cm.

CHAPTER 2 STREAM CHANNEL DETECTION USING MATHEMATICAL MORPHOLOGY

2.1 C-Star Algorithm

2.1.1 Basic Algorithm

Raw ALSM data comes in the form of an irregularly spaced “cloud” of discrete laser returns. Each point is associated with a 3D coordinate. The ALSM point cloud data is first segmented into ground and non-ground points using the method developed by Kampa and Slatton (Kampa *et al.*, 2004). The term “non-ground points” refers to laser returns from the foliage, light poles, or any houses or other structures in the forest that occlude the ground. The set of ground points is then interpolated to yield a bare-ground DEM or elevation image. Before applying the stream detection algorithm to the data, the georeferenced elevation values in meters are converted to gray level values from 0 to 255. This input elevation image is smoothed by convolution with a 7×7 disk-shaped (i.e. radius 3) structuring element (SE), (see Figure 2-1). We will discuss how we choose the size and shape of SE in Sections 2.2 and 2.3. Then, the Log Transformation and contrast stretching (i.e. histogram normalization) is used (Equation 2-1).

$$s = c \log(1 + r) \quad (2-1)$$

where c is constant (here $c=1$), and the input r represents the elevation values of the pixels after converting to gray-level (i.e. 0-255). This transformation maps a narrow range of low gray-level values in the input image into a wider range of output levels. Thus, the small variations in elevation between stream channels and the surrounding stream banks are emphasized in the resulting image s .

Morphology theory (Goutsias *et al.*, 2000) has been effectively applied in image processing for many purposes, including feature extraction. In grayscale morphology theory,

two fundamental operations (dilation and erosion) for an image f (Gonzalez *et al.*, 2002, Soille 2002) are defined as follows:

$$\begin{aligned}
 & \textit{Dilation} : \oplus \\
 & (f \oplus b)(s, t) = \max \{ f(s - x, t - y) + b(x, y) \\
 & \quad \forall (s - x, t - y) \in D_f; (x, y) \in D_b \}
 \end{aligned} \tag{2-2}$$

$$\begin{aligned}
 & \textit{Erosion} : \ominus \\
 & (f \ominus b)(s, t) = \min \{ f(s + x, t + y) - b(x, y) \\
 & \quad \forall (s + x, t + y) \in D_f; (x, y) \in D_b \}
 \end{aligned} \tag{2-3}$$

where D_f and D_b are the domains of image f and structuring element b , respectively, (s, t) are the row and column pixel indices in f , and (x, y) are the indices in b . From these basic operations, we can define additional operations.

$$\begin{aligned}
 & \textit{Opening} : \circ \\
 & f \circ b = (f \ominus b) \oplus b
 \end{aligned} \tag{2-4}$$

$$\begin{aligned}
 & \textit{Closing} : \bullet \\
 & f \bullet b = (f \oplus b) \ominus b
 \end{aligned} \tag{2-5}$$

The “bothat” operation is defined as the closing of the image minus the image. The term bothat is short for bottom-hat, which is so named because it is the inverse of the better known top-hat operation. It emphasizes local minima in pixel values at the scale of the SE.

$$\begin{aligned}
 & \textit{Bothat} : \\
 & h = (f \bullet b) - f
 \end{aligned} \tag{2-6}$$

The bothat morphological operator (Gonzalez *et al.*, 2002) is then applied using the same disk-shaped SE to isolate stream features. In many urban watersheds, roads are present in the imaged areas, in addition to streams. So it is important that the stream detection algorithm not be prone to detecting roads. In our data sets, roads are not detected by this algorithm because they do not exhibit as much variation in elevation as do streams. The result of this step is an image

that emphasizes the stream positions as local maxima, but it has a very low contrast. Histogram equalization is therefore performed to exaggerate the pixel value range. The stream channels are finally segmented from the surrounding terrain by applying Otsu's method (Otsu, 1979) to the grayscale image to form a binary image that depicts the two classes "stream" and "non-stream". Otsu's method is a simple unsupervised clustering method that finds the pixel value threshold that maximizes the distance between the two resulting pixel value clusters. Therefore, their combined spread (intra-class variance) is minimal. The resulting binary image contains the detected streams, but it also contains a small number of short "stray" regions, a common artifact of morphological filters and edge filters. The "stray" regions are not streams because they do not satisfy the criterion for the minimum size of a stream. These are removed using the simple "area" binary morphological operator that removes connected pixel groups of insufficient area. In this work, the DEMs are gridded to a pixel size of $1 \text{ m} \times 1 \text{ m}$, and the minimum area considered for a detected stream segment is based on general stream physical dimensions. To precisely locate the streams, the centerlines are then found using the thinning algorithm in (Gonzalez *et al.*, 2002). Thinning is the process of changing a large group of pixels into a single, one-pixel wide line. It preserves the Euler number (E): the number of holes (H) and connected components (C) in a figure, $E=C-H$. Figure 2-2 shows Hogtown Creek DEM of each process in C* algorithm.

2.1.2 Connecting Stream Segments

Because locally dense foliage can preclude ALSM returns from reaching the ground over small areas, it is possible to have some breaks in the detected stream paths. For flow routing, however, hydrologists desire unbroken stream paths. Therefore, we must link the stream segments. Several image processing approaches have been developed to link edges or contours in images (Dillabaugh *et al.*, 2002). In classic edge linking, it is often assumed that two

disconnected lines have the same orientation or direction. However, for connecting irregular pixel paths, such as stream centerlines, we use a more general notion of connectedness. We use Connectivity Number (CN) to join disconnected stream centerlines. In the binary image, the CN of the stream pixel is given one of five values: CN = 0: inner point, CN = 1: end point, CN = 2: connected point, CN = 3: branch point, and CN = 4: cross point (Japan Industry Technology Center, 1993).

In binary images, the Connectivity Number of the black pixel (i.e. values = 1) is the number of the connected black pixels in the neighborhood of the considered pixel. There are two kinds of connectivities: the 4-connectivity (horizontal and vertical directions) and the 8-connectivity (horizontal, vertical, and two diagonal directions). The 8-connectivity gives better visual performance with irregular paths. Therefore, only the 8-connectivity is discussed here and is defined in Equation 2-7 (Japan Industry Technology Center, 1993). See also Figure 2-3.

Connectivity Number (8-connectivity):

$$N_C^{(8)}(x_0) = \sum_{x_k \in S_1} (\bar{f}(x_k) - \bar{f}(x_k)\bar{f}(x_{k+1})\bar{f}(x_{k+2})) \quad (2-7)$$

where $S_1 = \{1,3,5,7\}$, $\bar{f}(x_i) = 1 - f(x_i)$, $x_0 = x_1$.

For the criteria of the connecting process, distances between end points are used. The distances between all end points are calculated. Each end point is associated with its nearest neighbor end point which is not in the same 8-connected label. If these end points are within a user defined bound (15 meter in this case), they become candidates for linking. The criterion of 15 m comes about because of the occlusions in the LiDAR point cloud induced by tree canopies. 15 m is approximately three times the smallest stream widths and is also the approximate maximum diameter of dense clumps of inter-mingled tree canopies. Where these clumps occur, very few LiDAR points reach the ground, and therefore the stream is not detected. The

candidate end point pair is then connected by the A-star algorithm (Fischler *et al.*, 1981), which is described below.

Connection Condition Rules:

- i. For each end point in the end point list, find all end points within distance D (where D=15m).
- ii. Of those candidates, find the closest end point that is not in same stream line (i.e. same label).
- iii. Then connect them by the A-star algorithm.

In computer graphic theory, ‘A-star’ is a best-first graph search algorithm that finds the least-cost path from a starting point to an ending point to be linked. It allows non-straight-line links. Before applying A-star, we generate a “Cost Image” (Equation 2-8) to reveal the similarities between the input image and the average of the detected stream pixels. In the Cost Image, a small pixel value indicates a higher possibility of being a stream pixel. Therefore, A-star finds the least-cost path through the Cost Image, finding the channel path with minimal error cost.

$$\text{Cost Image} = |\text{Input Image} - \text{Average of detected stream's pixels}| \quad (2-8)$$

where the input image is connecting area of elevation image and the average of all detected stream pixels is a scalar value.

Figure 2-4 depicts how we can employ the Cost Image to find the minimum-cost path connecting two pixels, i.e. the Starting Point (S) and Ending Point (E). In this process, two images, the Cost Image and a Step Image, are used. The Step Image shows the cumulative minimum cost of the path leading to the next pixel on the path from S.

First, every pixel in the Step Image is set to infinity, except for the S position. At the S position in the Step Image, we input the corresponding pixel value of the Cost Image. In each iteration of the Step Image, we sum Cost Image pixels in pixels adjacent to the current pixel in the 8-connectivity directions (i.e. horizontal, vertical, and two diagonal directions) and follow the path resulting in the lowest sum. We replace the infinity values in Step Image with the path sum values. When the pixel value of the E position in Step Image is reached and replaced with a finite value, the process stops. We then trace back from E to S following smallest values to find the minimum-cost path in the final Step Image. Figure 2-5 shows the connection results of DEM_{DS} over the Hogtown study site. It is better to use A-star rather than pure gradient (like D8) because the LiDAR typically hits trees between stream points and those points will be higher than the stream. Actually they may be not downward gradient. Therefore, A-star is better since it looks at a cost image (both positive and negative differences).

From this point on, we will refer to the entire process of detecting and connecting stream channel segments given a DEM as the C* algorithm, signifying the first complete generation of a channel extraction operator C* suitable for high-resolution LiDAR-derived DEMs.

2.2 Filter Parameter Selection using Simulated Terrain

The shape and size of the SE is very important in mathematical morphology. Therefore, after developing the basic algorithm to detect stream centerlines, a sensitivity analysis was performed with respect to the shape and size of the SE.

2.2.1 Simulated Data

We generate simulated elevation images using a 2D fractal process and embed meandering stream channels of different widths and depths (see, for example, Figure 2-6). We then calculate a nominal ALSM scan pattern over this terrain and randomly remove 80% to 90% of these simulated ALSM points to mimic the occluding effects of a dense forest canopy. The remaining

samples represent the ground points and are interpolated to simulate a bare-surface DEM obtained from ALSM data over forested terrain.

2.2.2 Error Metrics

The output of mathematical morphological operators strongly depends on the SE size and shape. Therefore, we needed to analyze the algorithm's performance over the simulated data as a function of SE size and shape via four Error Metrics (EM) enumerated as EM1 – EM4.

Our stream detection algorithm can make two kinds of errors: false negatives and false positives. A false positive occurs when the code classifies a detected stream centerline pixel as belonging to the stream class but the true stream centerline does not pass through that location. A false negative is when the code fails to classify a pixel as “stream” even though the true stream centerline passes through that location (See Figure 2-7). Let “×” in Figure 2-7 denote a pixel that was detected (classified) as a stream centerline pixel by the algorithm, and “○” denote a pixel that is on the true stream centerline. We associate each “×” with the nearest “○” (nearest neighbor rule). This will establish a one-way 1-to-1 correspondence between detected stream centerline pixels and true stream centerline pixels. For each of these “×-○” pairs, we compute the straight line (Euclidean) distance between them in 2D as

$$d_{\times\circ\min} = \sqrt{(\Delta x_{\times\circ\min})^2 + (\Delta y_{\times\circ\min})^2} \quad (2-9)$$

We then label all “×”s outside of a defined band around the true stream centerline of width 2τ (i.e. $d_{\times\circ\min} > \tau$) as false positives. Based on the known ALSM resolution and nominal stream sizes, we set the width parameter τ of this search band to be 5 m.

EM1 is the total number of false negative pixels, N_{fn} . There is no distance associated with this error measure since there is no detected stream centerline pixel in this case. The true stream

centerline pixels that have no corresponding detected pixel within the $\pm \tau$ -band are simply counted.

EM2 is the total number of false positives, N_{fp} . These are simply the “×” pixels that lie outside of the $\pm \tau$ -band. No distance is associated with this measure since closeness does not count if the “×” is outside of the $\pm \tau$ -band.

For those detected points that remain, i.e. for “×” pixels that lie inside the $\pm \tau$ -band, we sum the distances to the nearest “○”. It is possible to have a false positive inside the $\pm \tau$ -band, however, we will not consider that an error since τ was chosen small to tightly conform to the stream. This gives $\sum |d_{xo\min}| / N_{TD}$ for EM3, where N_{TD} is the number of true detected pixels. This is simply the mean absolute error.

For EM4, we simply define the sum of these three errors, normalized by the number of pixels in the true stream centerline N_o .

$$EM4 = (N_{fn} / N_o) + (N_{fp} / N_o) + (\sum |d_{xo\min}| / N_{TD}) \quad (2-10)$$

2.3 Simulation and Real Data Result

2.3.1 Simulated Data Result

Figure 2-8 and Figure 2-9 show detection results of simulated data. Figure 2-8 is the same data which is shown in Figure 2-6 and is used to calculate Error Metrics. In Table 2-1, we see that larger SEs result in more false positives (larger EM2) and are less likely to have disconnects in the stream (smaller EM1). In Table 2-2, we see the disk shape SE is more less sensitive to changes in stream direction, as implied by the low EM4 score. Different SEs were tested by varying its size and shape and it was found that the 7×7 disk-shaped (i.e. disk with radius 3) SE yields the smallest total error (EM4). The disk shape as a structure element has the property of being isotropic, i.e. the property of being independent to changes of orientation.

2.3.2 Stream Channel Detection in Real Data

While it is the 3D shape of the stream channels that C* is sensitive to, it is convenient to focus first on the detection results in a planform, or top view. The detection results of DEM_{G3} and DEM_{DS} over the Hogtown site are shown in Figure 2-10. The forest is predominantly in the eastern (right) portion of the image. Many shallow geometric features associated with roads and residential yards are visible in the western portion. The C* algorithm was designed to not detect roads (alternative algorithms are used for that purpose), so that in urban watersheds it does not confuse streams with roads.

The most striking feature in the DEMs is an almost rectangular shaped depression in the forested area. This is an old borrow pit, from which sand was extracted, when roads were expanded in this area many years ago. It has since become densely vegetated and exhibits a complex network of short channel forms, some natural and some modified intentionally. Such forms can make low-relief and urban watersheds particularly problematic to analyze with more traditional approaches based on contributing area, which is simply a method of counting the number of pixels that would drain water into a given pixel using the watershed algorithm (Beucher *et al.*, 1979). The D8 algorithm (Jenson *et al.*, 1988, and O'Callaghan *et al.*, 1984) is an example of this that is well known in the hydrologic literature. The C* algorithm readily detects these small channel forms. But for this study, the channels detected in that area are excluded so that focus may be placed on the two main stream channels: Possum Creek entering from the north and Hogtown Creek entering from the east. The two creeks merge near the southern edge of the DEM, below which it is simply referred to as Hogtown Creek.

In the DEM_{G3} (Figure 2-10), we see that the C* extracted stream channels agree very well overall with the hand digitized channels. True stream center line is made by hand watching DEM_{G3}. We checked accuracy of stream detection using Global Positioning System (GPS) at

discrete points. However, for continuous ground truth, we had to do hand digitized since GPS signal is not good enough under canopy to do kinematic GPS. A zoom view over the stream confluence reveals that agreement is often better than one meter in the main channel. In fact, the Mean Absolute Error (MAE) between the hand digitized main channel and the detected channel centerline is only 1.31m (each pixel is 1m×1m). However, in the zoom view we can see small “off shoots” from the main channel that are detected by the C* algorithm. Visits to the site revealed that these smaller channels are in fact real features and not algorithmic artifacts. These small incisions are often fewer than 6m long and only 1-2 m across. They tend to occur between the root balls of individual trees on this forested floodplain. We speculate that they may have formed in response to high runoff events when the floodplain experiences large volumes of standing water. As the water level over the floodplain recedes, water flows through these incipient incisions into the main stream. Given the density of understory and lower canopy foliage, these features are often not even visible to an observer until one has practically stepped into them, and therefore represent a dramatic advance in channel detection in forested watersheds from remote sensing platforms.

In the DEM_{DS} overview in Figure 2-10, we see that C* still manages to extract stream channels well overall, in spite of the lower LiDAR point density. The zoom view over the stream confluence reveals that agreement is better than a meter in much of the main channel. Also, many of the incipient incision features are still detected. The MAE between the detected channel centerline and the hand digitized channel (which is based on DEM_{G3}) is 1.54m. This rather small increase in MAE between DEM_{G3} and DEM_{DS} suggests that applying C* to other forested watersheds that were imaged with older NCALM data could also yield satisfactory stream extractions in planform. We do see in the zoom view of Figure2-10 that the narrow neck

of an isthmus in DEM_{G3} is detected as a channel in DEM_{DS} , thus changing the small isthmus to a small island.

Results from using the C* algorithm, detection results at two other study sites (Hatchett Creek in northern Florida and Red Wall Canyon in Death Valley) are shown in Figure 2-11 and Figure 2-12, respectively. Based on our stream detection results, C* algorithm gives good performance at all sites.

2.3.3 Features of Stream Channels

Most available ALSM measurements (including those from NCALM) are based on an Nd:YAG laser that emits pulses in the near-infrared (1064 nanometers) portion of the spectrum. The optical properties of water are such that light in the near-IR does not significantly penetrate below the water surface. Thus, these ALSM sensors cannot directly observe the true channel bottoms if water is present. In the Hogtown site during late winter and early spring, the water stage is often quite low (less than 20cm in places). Furthermore, in March 2007, this area was still experiencing a significant drought. So channel depths estimated from this particular LiDAR data set are likely to be within a few decimeters of the true bottom depth (except over small scour holes and fallen trees in the channel). The same is true for nearby Hatchett Creek and the very dry Red Wall Canyon in Death Valley. Thus, for the purposes of this work, the channel depth-to-the-water-surface measured by ALSM will be referred to as simply the depth.

With the channel centerlines extracted, it is straightforward to automatically extract the locally orthogonal channel cross-sections at every centerline pixel. Two extracted cross-sections are shown in Figure 2-13. The locations from which they originate are indicated in the DEM overviews in Figure 2-10. Cross-section (or transect) T1 comes from a relatively straight section of Possum Creek, whereas transect T2 comes from a pronounced meander bend in Hogtown Creek. One would generally expect the channel cross-section in the meander to exhibit greater

asymmetry between the outer and inner bank slopes based on typical erosion and sediment deposition patterns that arise from the fluvial processes that form and maintain the streams (Knighton, 1998). This is, in fact, revealed in the transects in Figure 2-13.

To compare between cross-sections of DEMs in real terrain, six cross-sections (four over straight portions of the streams and two over curved portions) were measured in the field using total station, which is an optical instrument used in modern surveying, at the Hogtown site. Each cross-section had more than twenty shots with distances between shot positions of about 20-50 cm. The MAE (Mean Absolute Error) between DEMs (DEM_{G3} , and DEM_{DS}) and survey results are 0.1212 m and 0.23 m, respectively.

Figure 2-14 shows two of the cross-section survey results using the total station and a 3D view of one of the cross-sections. It validates that our estimated cross-sections in DEM_{G3} are closer to the real terrain than DEM_{DS} , yet both DEMs lead to very good results when one considers the nominal absolute accuracy of LiDAR points stated earlier and the fact that this is obtained through dense forest canopy.

In spite of the close overall agreement between DEM_{G3} and survey elevations, care should be taken in any attempt to extract channel morphology at submeter scales from ALSM data because the point spacing on the ground is highly non-uniform due to the complex occlusions of the vegetation. Terrestrial (ground-based) LiDAR would be preferred when robust submeter channel form morphology is required in forested areas.

Relative errors in the cross-sections extracted from DEM_{G3} and DEM_{DS} were examined. In the case of the T1 transect, the relative MAE in elevation was only 11.3 cm and the standard deviation of the signed error was 15.6 cm. For transect T2, the relative MAE in elevation was only 21.3 cm and the standard deviation of the signed error was 20.8 cm. Based on survey

results, we know that the DEM_{G3} is very close to the real terrain. It may be that a 10 – 20 cm loss in precision from DEM_{DS} is significant for some fluvial morphology applications. In such cases, this result suggests that state-of-the-art high pulse rate ALSM data may be required along with C* to adequately extract channel forms. As a general rule of thumb, it would be reasonable to say that older LiDAR point densities (as in DEM_{DS}) are quite sufficient for general extraction of channels in planform, and that higher densities (as in DEM_{G3}) should be used when trying to extract 3D channel forms.

With the capability to now systematically extract channels in planform and in cross-section all along their paths, it becomes possible to characterize channel form parameters, such as Radius of Curvature (ROC), width, depth, and bank slope asymmetry \tilde{m} .

Normalized bank slope asymmetry was calculated as

$$\tilde{m} = \text{norm} \left\| |m_R| - |m_L| \right\| = \left| |m_R| - |m_L| \right| / \max \left(|m_R|, |m_L| \right) \quad (2-11)$$

where $|\tilde{m}|$ is the normalized bank slope asymmetry, m_R and m_L are the estimated slopes of the right and left banks, respectively.

Under normal fluvial processes, one generally expects an inverse relation between $|\tilde{m}|$ and ROC (Knighton, 1998). In other words, where there are sharp bends in the stream (small ROC), we expect larger slope asymmetry. In Figure 2-15, there are ten white circles. The numbers 1, 2, 5, 8, and 10 are at curved stream positions and the numbers 3, 4, 6, 7, and 9 are at straight stream positions. It shows the expected inverse relation between ROC and bank asymmetry except at number 8. The highest tree density occurs at number 8. This is quite interesting because it indicates that the presence of trees near the banks can modulate the expected channel forms. This is intuitive since the root balls of trees can be seen to retain much soil (see Figure 1-2). Nonetheless, this is a significant finding since most books on fluvial processes only consider the

case of streams in open terrain, where the sediment and erosion patterns are not modulated by vegetation.

Figure 2-16 shows 1-D plots of ROC, bank asymmetry, depth and width of Hogtown Creek following the stream from left to right in the DEM image. Width is similar throughout this entire stream segment and depth is increasing from right to left. The stream flows from right to left and merges with Possum Creek at the left. This explains why depth is larger on the left side (more runoff accumulates as you move further down stream). From distance indices 0 to 15, and 85 to 105 along the horizontal-axis, bank asymmetry values are unstable and a little bit higher. Also along this section, the tree density is high for a long interval. If tree density is low in short intervals, it does not appear to affect the inverse relation between ROC and slope asymmetry very much, but if it is low in a long interval, it has a larger affect on the bank asymmetry values (i.e. from 0 to 15 and 85 to 105 in horizontal-axis). From distance indices 180 to 190 along the horizontal-axis, the inverse relation is not strong, because the tree density is highest. Figure 2-17 shows 2-D figures of ROC, asymmetry of bank slope, depth and width following Hogtown Creek. We can easily find that ROC and slope asymmetry have an inverse relation.

Computing lengths of the small incipient channel features in DEM_{G3} yielded the following statistics: a detected mean value of 2.6m with standard deviation of 1.2m. Detected channels longer than 6m were not included so as to focus on the small incision features. Width and depth of these features were not estimated since the features are often only one or two meters wide and the DEM resolution was $1m \times 1m$. The length statistics could, however, prove very useful to hydrologists trying to characterize a channel network.

Flow speed and rate of the stream waters depend on the channel's characteristics. A channel's slope, size and surface roughness can all influence a stream's flow. The relationship between flow and these channel characteristics is shown in the Manning equation (or Manning's empirical formula, Gauckler, 1867), which is well known in hydrologic literature and can be adapted to determine both flow speed and flow rate. Manning's empirical formula for the mean cross section velocity of gravity-driven, uniform, fully developed turbulent flows in rough open channels is among the better known expressions used by hydrologists, geomorphologists, and hydraulic engineers (Gioia *et al.*, 2002). Lacking a better solution, it is assumed that the equation is also valid for non-uniform reaches that are invariably encountered in natural channels if the energy gradient is modified to reflect only the losses due to boundary friction (Dalrymple *et al.*, 1967). The formula is customarily used to determine the capacity of natural streams and flood plains, and to design artificial channels (Dooge, 1992 and Chow, 1988). It has also been used to quantify the vast flows which appear to have occurred on Mars in the distant past (Carr, 1979). Because it embodies a large body of experimental results (Dooge, 1992), and it produces good performance in general, Manning's formula offers a simple parameterization of channels useful for many applications. In spite of the fact that there is little detailed theory justifying Manning's formula, the following assertion, made in a classical text on geomorphology (Leopold *et al.*, 1964), remains accepted after thirty-seven years: "It is truly surprising that engineering practice has depended to such an extent on a formula as empirical as this one, derived nearly a century ago" (Gioia *et al.*, 2002). Manning's formula is written as:

$$V = \frac{k}{n} R^{\frac{2}{3}} \cdot S^{\frac{1}{2}} \tag{2-12}$$

$$Q = \frac{k}{n} R^{\frac{2}{3}} \cdot S^{\frac{1}{2}} \cdot A \quad (2-13)$$

where V is the velocity (m/s), Q is the flow rate (m^3/s), k is a conversion constant equal to 1.0 for International System of Units (i.e. SI units), n is the Manning coefficient of roughness (independent of units), A is the cross sectional area of flow (m^2), P is wetted perimeter (m), R is the hydraulic radius (m) given by $\frac{A}{P}$, and S is the along-track slope of the water surface or the linear hydraulic head loss. Appropriate values of n have been measured for different types of channel walls, and tabulated (Chow, 1988).

For Hogtown Creek, we assumed it approximates a rectangular open channel, water is fully loaded in channel shape with a Manning coefficient of 0.035 for the winding (meandering) stream or rivers. The resulting calculated Hogtown stream velocity is 1.9046 (m/s) and flow rate is 11.5986 (m^3/s). It was not possible to verify these velocity estimates since it would require placing flow meters *in situ* (which we do not have) into the stream and field expertise for making such measurements. Yet, we have demonstrated for the first time that the high resolution channel widths and depths derived from the LiDAR data can now be used in conjunction with Manning's formula to produce such estimates.

0	0	1	1	1	0	0
0	1	1	1	1	1	0
1	1	1	1	1	1	1
1	1	1	1	1	1	1
1	1	1	1	1	1	1
0	1	1	1	1	1	0
0	0	1	1	1	0	0

Figure 2-1. A 7×7 disk-shaped binary structuring element.

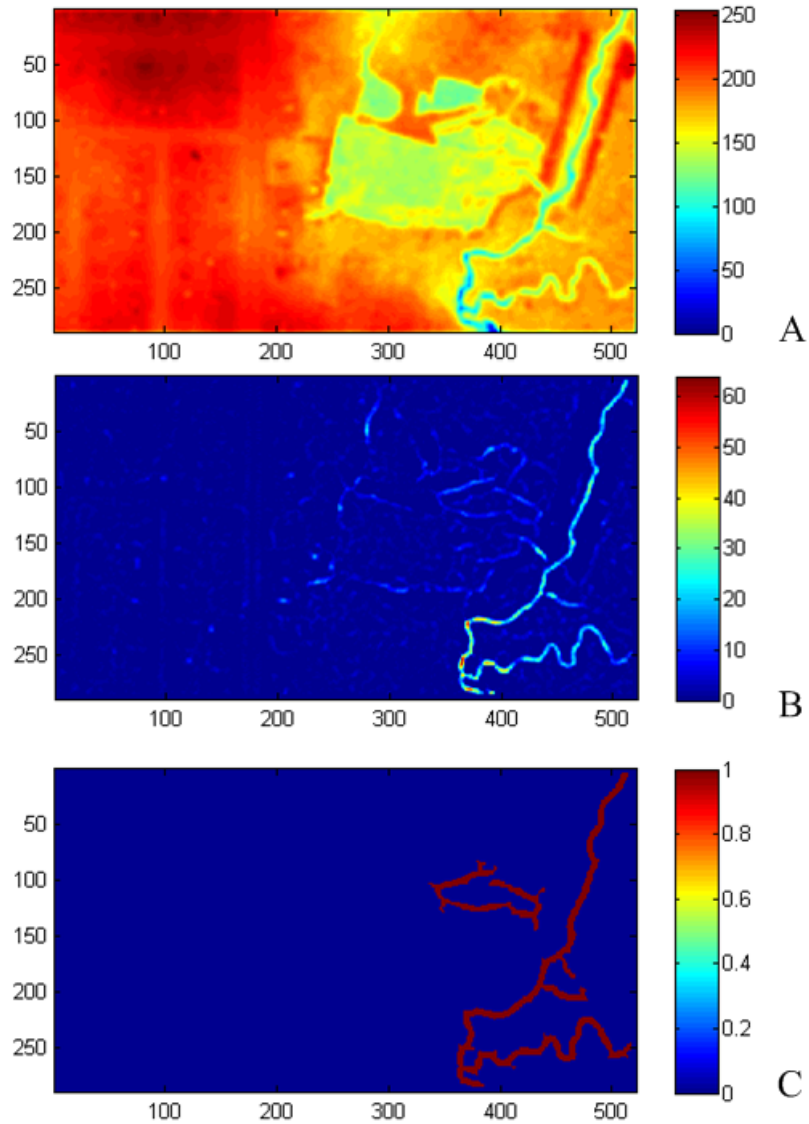


Figure 2-2. Hogtown Creek DEMs of each process in C* algorithm. A) After log transform and contrast stretching. B) After both that operation. C) After Otsu's method.

$x_4 (i-1, j-1)$	$x_3 (i-1, j)$	$x_2 (i-1, j+1)$
$x_5 (i, j-1)$	$x_0 (i, j)$	$x_1 (i, j+1)$
$x_6 (i+1, j-1)$	$x_7 (i+1, j)$	$x_8 (i+1, j+1)$

Figure 2-3. The 3x3 pixel neighborhood used in the eight-connectivity algorithm.

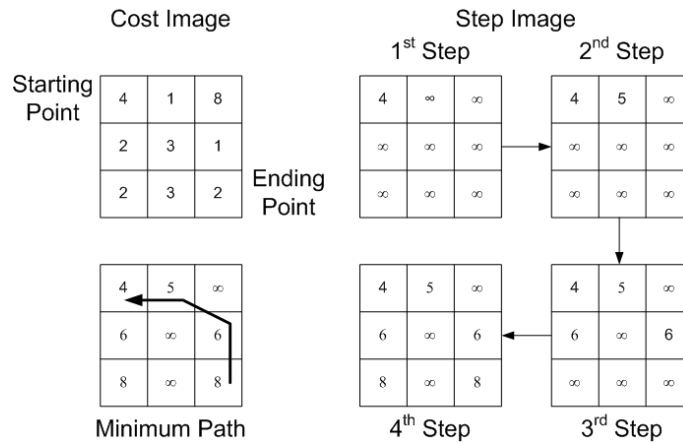


Figure 2-4. Minimum-cost path extraction process for a 3 x 3 image. The cost image is in the upper left. The starting point (i.e. 4) and ending point (i.e. 2) are shown. The steps are continued until the goal pixel is added in the process. Once the ending point is reached, a path is traced back from the ending point to the starting point following the smallest values to find the minimum-cost path

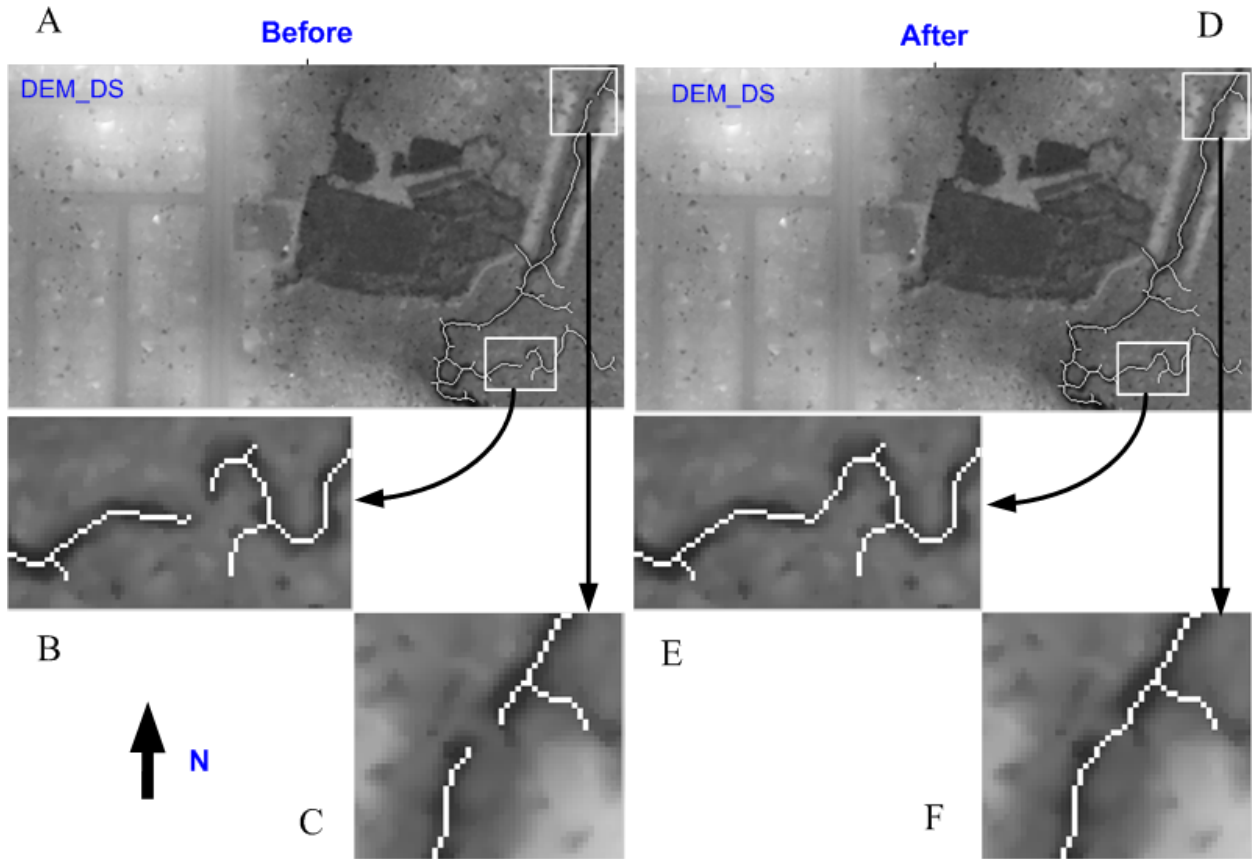


Figure 2-5. The connection results of DEM_{DS} over the Hogtown site. Detection results before applying connecting algorithm (A, B, and C). Detection results after applying connecting algorithm (D, E, and F).

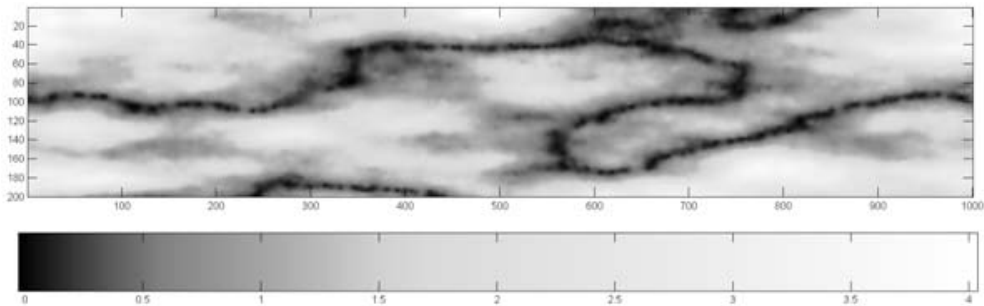


Figure 2-6. Simulated DEM of a 200m×1000m ALSM imaging swath over a meandering stream. Elevations are in meters and pixel size is 1m×1m. Minimal topographic relief is used to simulate a Florida flood plain test site. Bright pixels are high elevations, whereas dark pixels are low elevations.

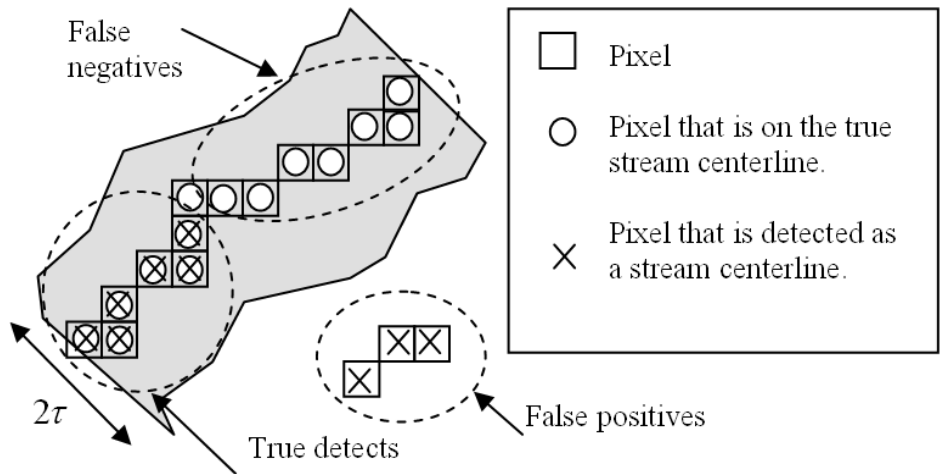


Figure 2-7. Definitions of detection errors. The gray area represents a thin band around the stream center line of width 2τ .

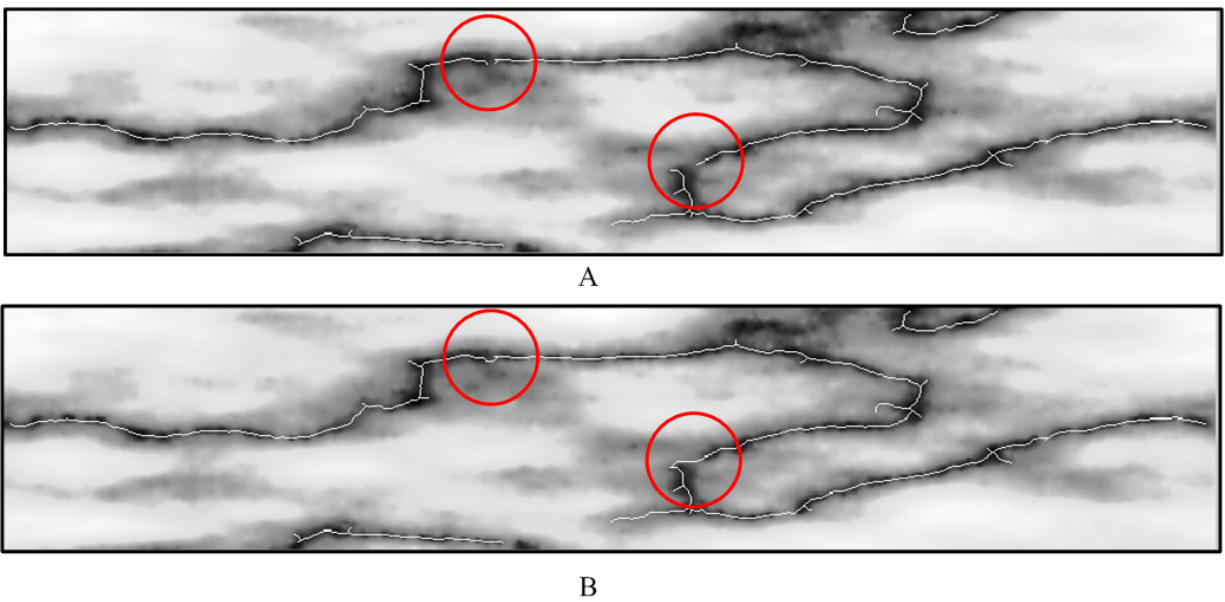


Figure 2-8. Testing algorithm on simulated terrain. A) Simulated DEM of a $200\text{m} \times 1000\text{m}$ ALSM imaging swath over a meandering stream before applying connection algorithm. B) Simulated DEM with detected channel center line (white line) after applying connection algorithm. Connected stream segments are indicated by red circles.

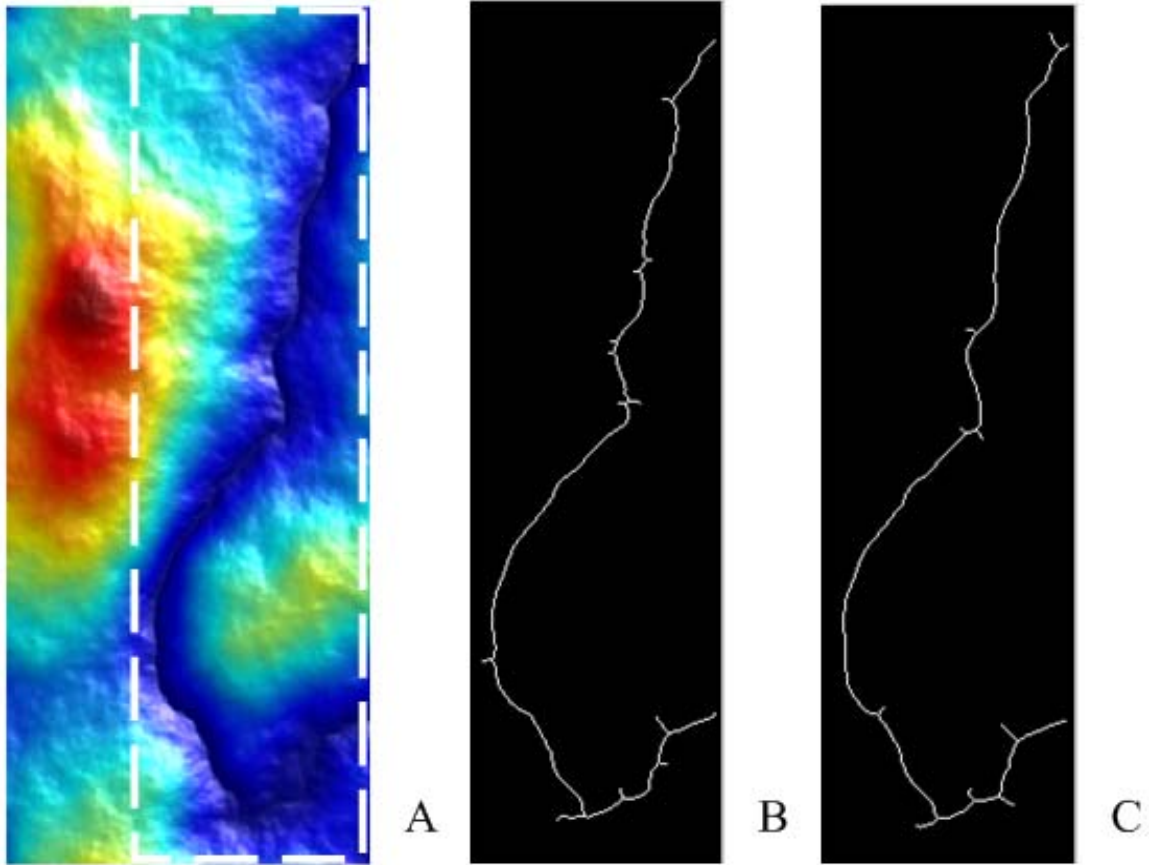


Figure 2-9. Testing algorithm on another simulated terrain. A) Simulated small meandering stream in low-relief terrain (1000m×200m). It is a 1m x 1m fractal surface with embedded channel. B) True path of the simulated stream. C) Detected channel center line. Mean absolute error between true and detected channel centerline pixels is only 0.32 pixels.

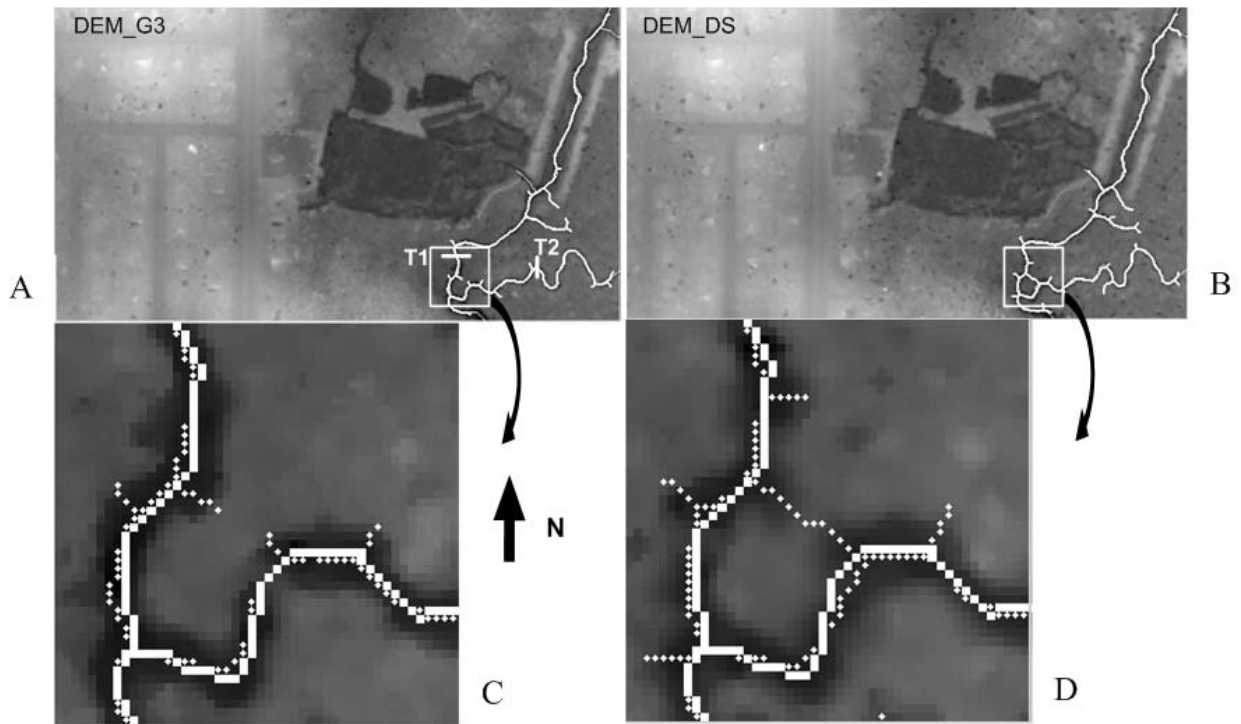


Figure 2-10. Planform channel detection results at the Hogtown Creek. A) DEM_{G3} showing the true (hand digitized) main channel (solid line) and the channel detected by the C^* algorithm (dotted line). Very little difference is visible in the overview, suggesting good performance overall. The imaged area is $290m \times 521m$ with $1m \times 1m$ pixels (total elevation range is 7 meters). B) DEM_{DS} showing the true main channel (derived from DEM_{G3}) and the detected channel derived from running C^* on DEM_{DS} . Overall performance is still quite good. C) A $47m \times 46m$ zoom view onto a channel confluence from the top left result. D) Corresponding area from the top right result. At this scale, detection differences between the DEMs become apparent.

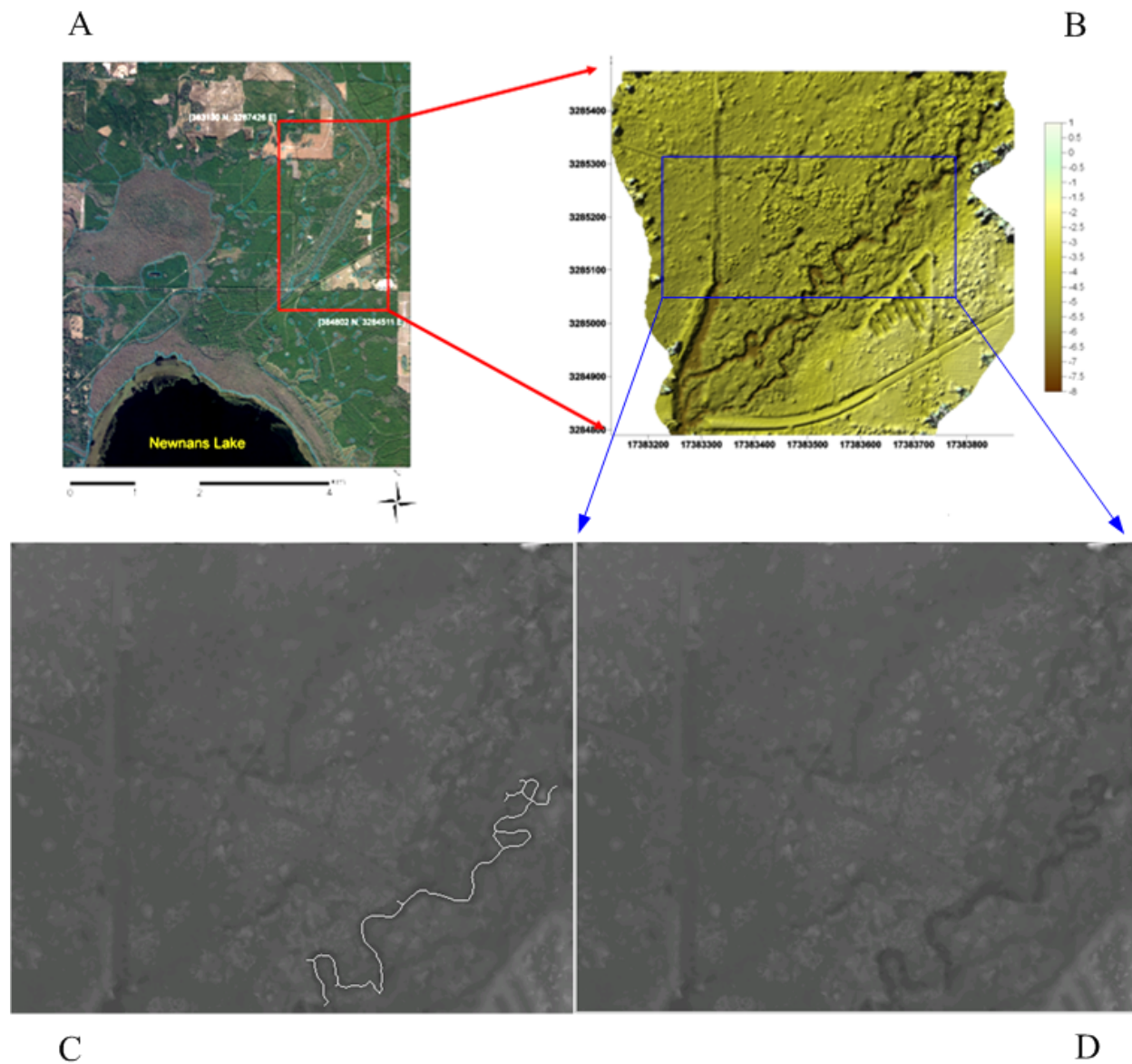


Figure 2-11. A) A satellite image of the Hatchett Creek area near the Gainesville Regional Airport from Google Earth. B) A bare-surface DEM of the Hatchett Creek, FL site. C) Detection result of the C* algorithm. D) The same area as in “C”, without the detected stream (425 m x 510 m, 1m×1m pixels, and total elevation range is 7 meters) for comparison.

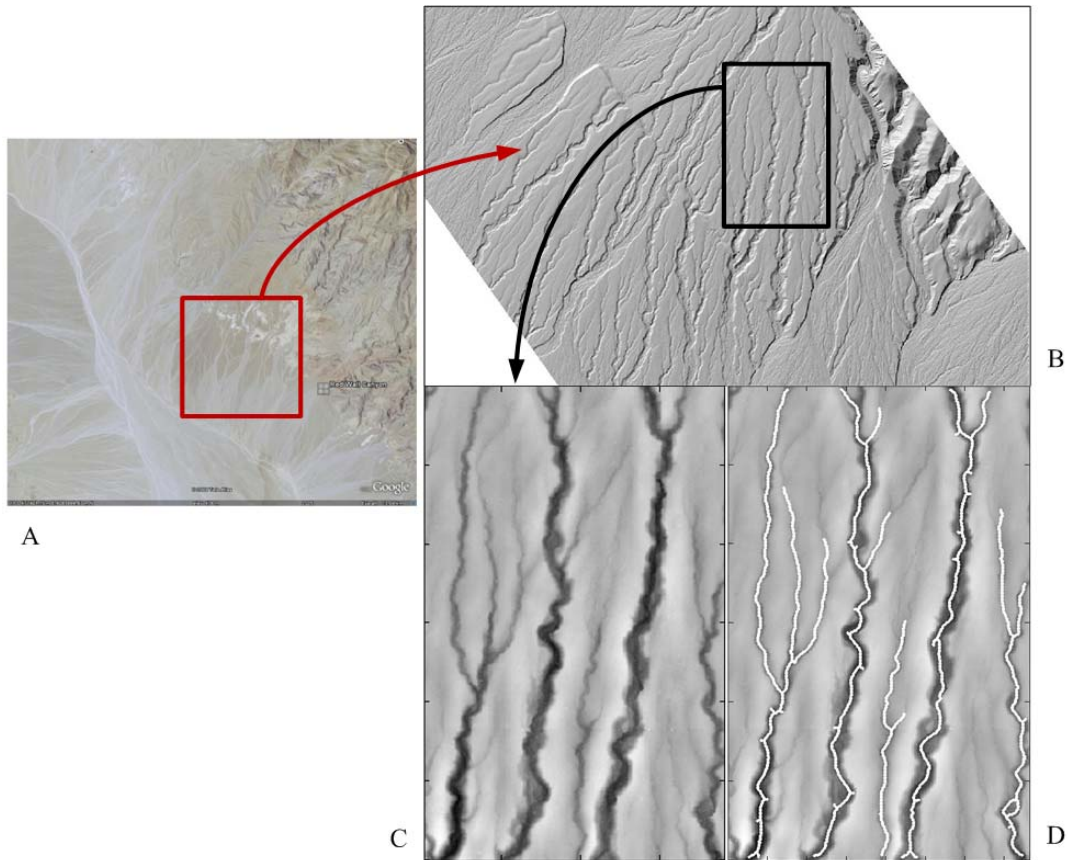


Figure 2-12. A) A satellite picture of Red Wall Canyon in Death Valley, CA from Google Earth. B) a zoom view of the area showing the bare-surface DEM derived from LiDAR. C) a further zoom in to show channel details. D) Detection result of C* algorithm (601 m x 382 m, 1m×1m pixels, and total elevation range is 90 meters). Although Death Valley is very dry, short flood events known as cloud bursts can result in channel formation in the soil.

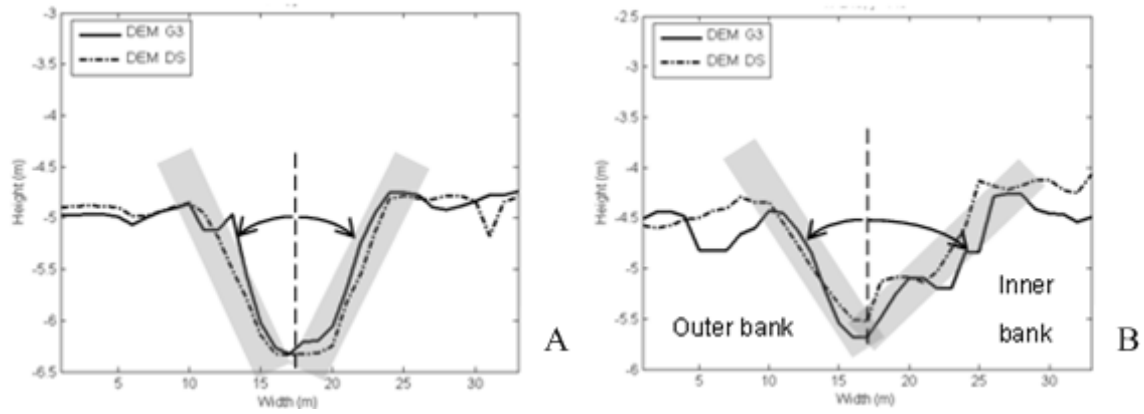


Figure 2-13. Stream channel cross-sections. A) A comparison between the cross-sections automatically extracted from location T1 in DEM_{G3} and DEM_{DS} from Figure 2-10. B) A similar plot for location T2 from Figure 2-10. In this case, the bank slopes clearly display more asymmetry in “B”, which is often associated with bends in meandering channels in which erosion dominates the outer bank and deposition dominates the inner bank. The detection algorithm enables the systematic “mining” of the DEM data to detect asymmetric portions of the channel.

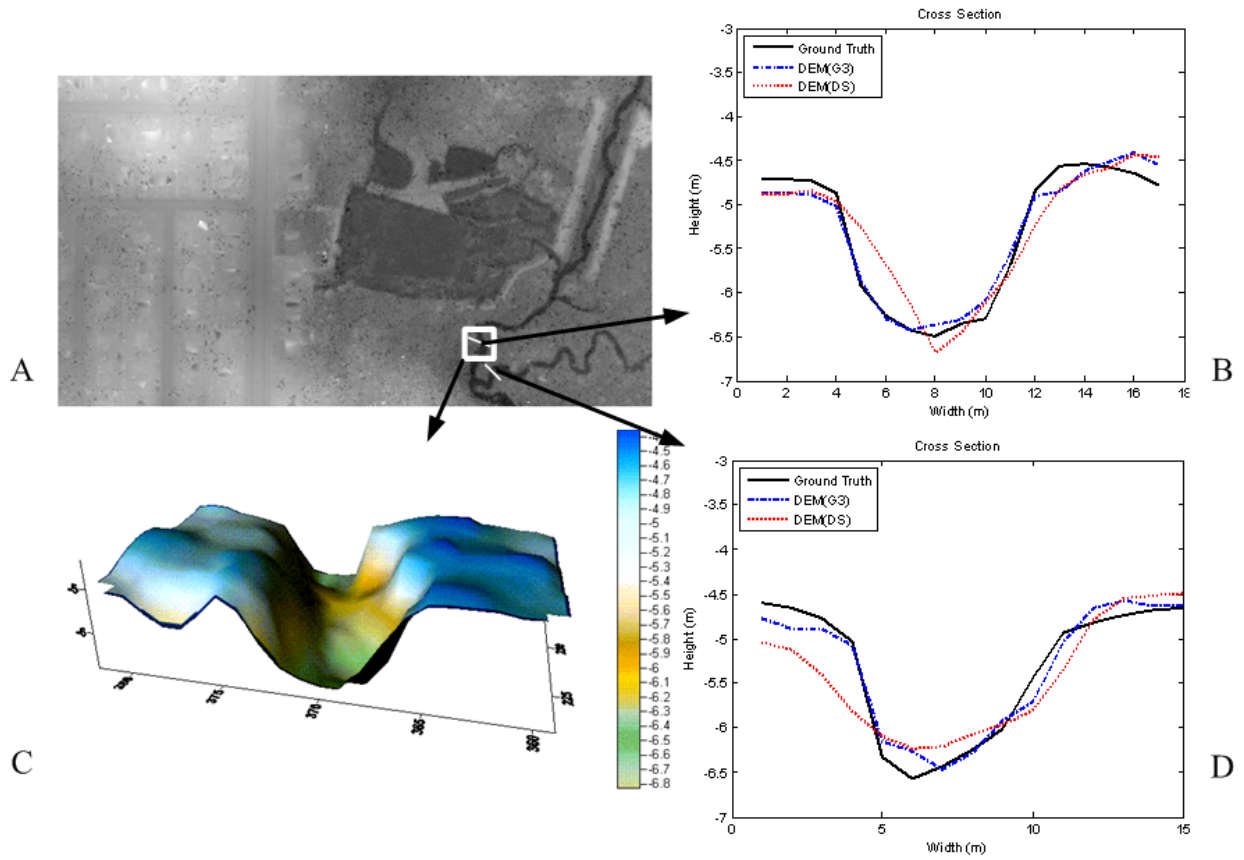


Figure 2-14. Cross-sections of survey result, DEM_{G3} and DEM_{DS} in Hogtown Creek (B and D). Both right figures show DEM_{G3} is closer to the survey result than DEM_{DS} . C) 3D cross-section view of white rectangular area.

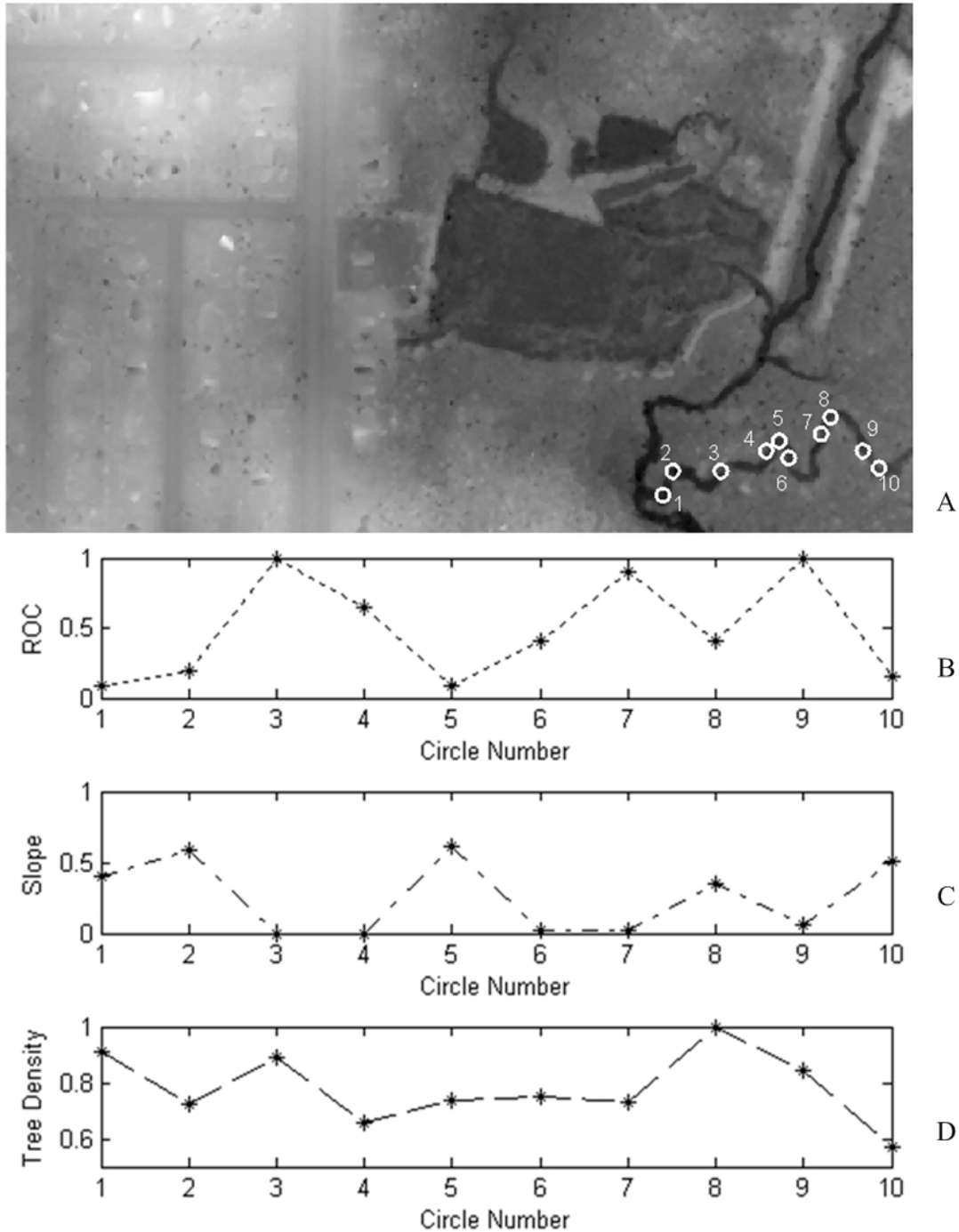


Figure 2-15. Results of ROC, bank slope asymmetry and tree density in DEM_{G3} . A) Small white circles show the positions along Hogtown Creek where ROC, bank slope asymmetry, \bar{m} and tree density were calculated in DEM_{G3} . Numbers 1, 2, 5, 8, and 10 are at curved stream positions and numbers 3, 4, 6, 7, and 9 are at straight stream positions. B) The plots of normalized ROC. C) Normalized bank slope asymmetry. D) Normalized tree density.

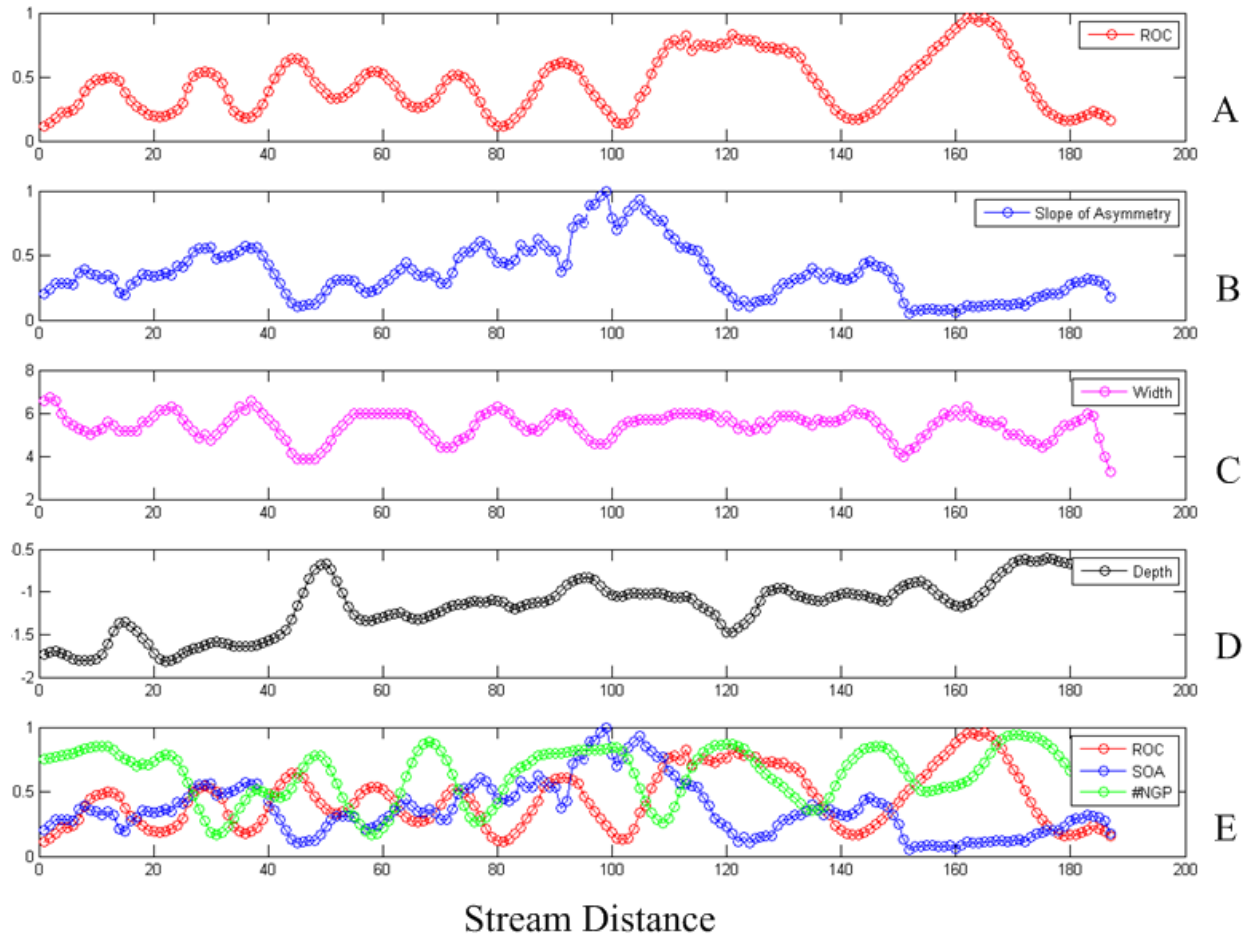


Figure 2-16. 1-D plots of Hogtown Creek features. A) ROC. B) Bank asymmetry. C) Width (*m*). D) Depth (*m*). E) A superposition plot of ROC (red), bank asymmetry (blue), and tree density (green).

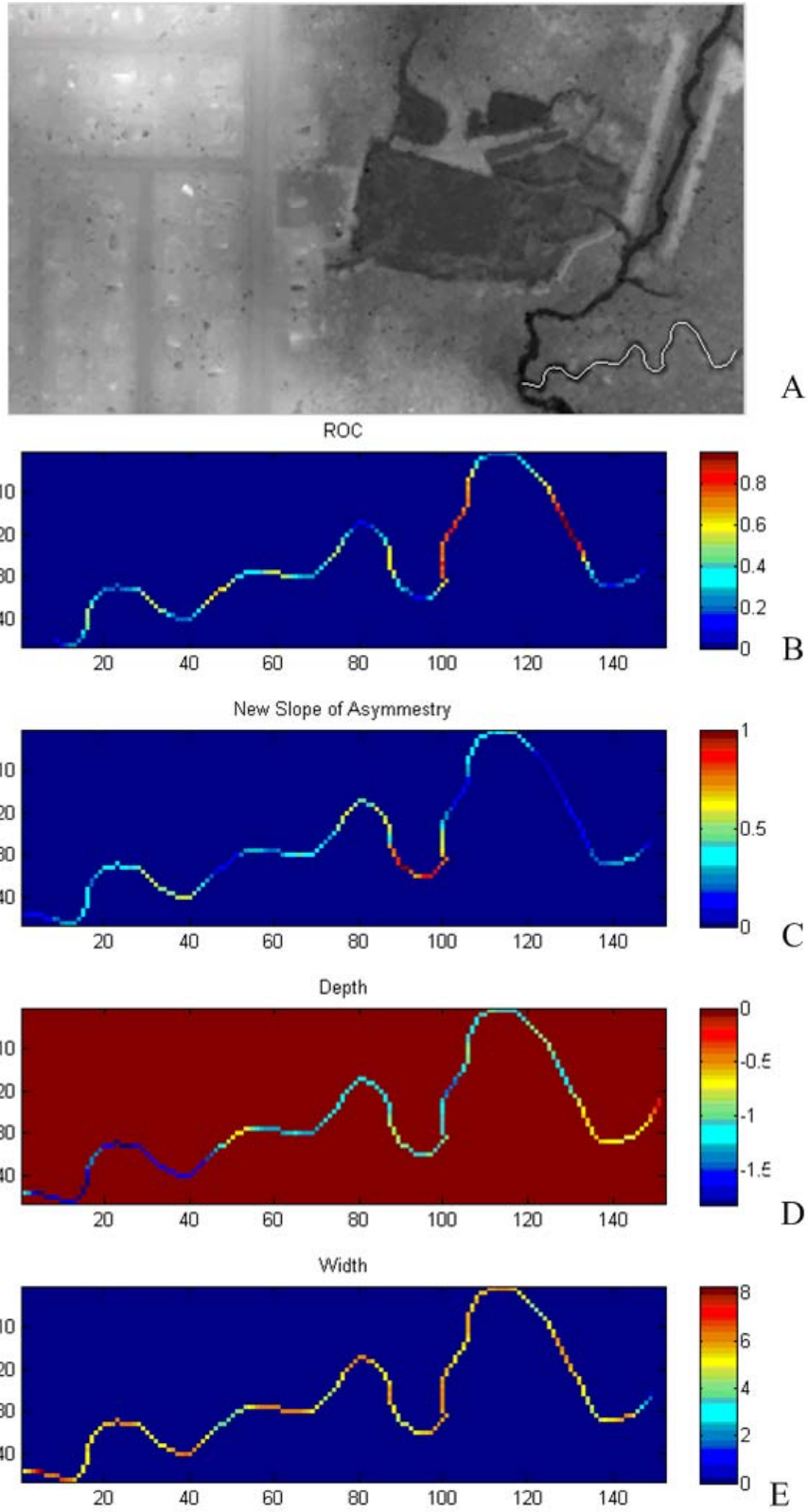


Figure 2-17. 2-D figures of Hogtown Creek features. A) Hogtown Creek. B) ROC. C) Bank asymmetry. D) Depth (m). E) Width (m).

Table 2-1. Error metrics vs. sizes of disk shape SE for simulated data

	EM 1	EM2	EM3	EM4	N_{TD}
Radius 2 (5 by 5)	785	18	1.6843	2.0722	1222
Radius 3 (7 by 7)	581	22	1.6713	1.9626	1406
Radius 4 (9 by 9)	588	130	1.8277	2.1601	1473

N_o : 2070 (Number of pixels in the true stream centerline)

N_{TD} : Number of true detected pixels

Table 2-2. Error metrics vs. shapes for the “best” size of 7×7 for simulated data

	EM 1	EM2	EM3	EM4	N_{TD}
SE Rectangle (3 by 7)	1559	7	1.5676	2.3241	535
SE Diamond (7 by 7)	655	22	1.7072	2.0342	1347
SE Square (7 by 7)	545	97	1.7855	2.0956	1483
SE Disk (7 by 7, Radius 3)	581	22	1.6713	1.9626	1406

N_{TD} : Number of true detected pixels

CHAPTER 3 STREAM AND ROAD DETECTION USING DIFFERENTIAL MORPHOLOGICAL PROFILES

3.1 Background of Differential Morphological Profiles

Opening and closing are commonly used in morphological operations because, unlike dilation or erosion alone, they generally maintain the size of the features in the image. The open operation dilates an eroded image, whereas the close operation erodes a dilated image. The morphological top-hat operator for grayscale images is also a well known morphological operator. Its function is to detect local maxima on non-uniform backgrounds. The top-hat is the difference between an image f and its opening, i.e. $tophat(f) = f - f \circ b$, which extracts bright structures or large pixel values. The bothat operator was mentioned in Chapter 2. It is the difference between image f and its closing, $bothat(f) = f \bullet b - f$, and it extracts dark structures or small pixel values (i.e. local minima).

Regardless of the particular morphological operation, the response of an image object to that operator depends strongly on the SE. A simple structure of a particular size may have a high response for one SE size, and a low response for other SE sizes. For example, consider a DEM image of a large bowl-shaped depression that is 200 pixels in diameter. While the center of that bowl is certainly a local, if not a global minimum, a bothat operator defined on a SE that is 10 pixels wide will respond to small random fluctuations in the elevations rather than to the large topographic depression.

In some applications, such as photographic inspection of parts in a factory, the sizes of the structures to be detected are known. Another example is that shown in Chapter 2, in which a small urban flood plain was studied and most of the main stream channels were of similar widths. But in the general case where large complex landscapes are imaged, it is not always possible to

know the size of the channels in advance. Furthermore, no single SE size may adequately detect all of the channels if they vary greatly in width. Therefore, in such cases, a multi-scale approach based on a range of different SE sizes is appropriate. A range of different hypothetical spatial domains is analyzed, and the highest (best) response of the structures in the image is used for the classification procedure.

The idea to use a composition of opening transforms for a morphological segmentation of satellite data was originally proposed for the detection of different urban structures in (Bianchin *et al.*, 1994) and (Pesaresi, 1993). By the simple arithmetic addition of a series of openings with an increasing SE, segmentation labels were acquired in the method in (Bianchin *et al.*, 1994) and (Pesaresi, 1993). Those methods are only useful to binary images, and the geodesic metric is not used. In Pesaresi *et al.* (1999), a composition of geodesic opening and closing operations of different sizes for building a morphological profile is applied. In Pesaresi *et al.* (2001), Pesaresi and Benediktsson suggested the differential composition of geodesic opening and closing operations of different sizes, which are both more general and more robust than the methods in (Bianchin *et al.*, 1994), (Pesaresi, 1993), and (Pesaresi *et al.*, 1999). Since the tophat and bothat operations are efficient segmentation tools for extracting bright and dark, respectively, objects from an uneven background, we replace opening and closing with tophat and bothat operations for our work. We refer to the differential composition of geodesic tophat and bothat operations of different sizes as Morphological Profiles (MPs). We then apply Differential Morphological Profiles (DMPs) to the classification of landforms in the DEMs. It is first time that the tophat-bothat filters have been employed with DMPs.

A potential disadvantage of these methods (MPs or DMPs) is that they can lead to large feature sets because a series of tophat and bothat operations occur. The MP method produces an

image feature set which can help classify the feature data very effectively, but it also leads to many redundancies in the feature set. Thus, we would like to see if the MP and DMP feature selection can be combined with feature reduction to help to find the most important features in the feature space and if similar classification performances can be acquired with a reduced feature set. We will use two feature extraction methods: Principal Component Analysis (PCA) and Linear Discriminant Analysis (LDA). After feature extraction, Bayesian classification will be used to classify the data assuming Gaussian distribution.

3.2 Differential Morphological Profiles

The Morphological Profiles (MPs) and their derivatives, the Differential Morphological Profiles (DMPs), are used to create a feature vector from a single image I . Both methods are based on the repeated use of, in our case, the tophat and bothat operators. A Morphological Profile is comprised of the tophat profile (TP) and the bothat profile (BP). The TP at pixel x of image I is defined as an n -dimensional vector:

$$TP_i(x) = \tau_R^{(i)}(x), \forall i \in [0, n] \quad (3-1)$$

where $\tau_R^{(i)}$ is a morphological tophat operator by reconstruction using structuring element (SE) of size i , and n is the total number of tophats. Also, the BP at pixel x of image I is defined as an n -dimensional vector:

$$BP_i(x) = \beta_R^{(i)}(x), \forall i \in [0, n] \quad (3-2)$$

where $\beta_R^{(i)}$ is a morphological bothat operator by reconstruction with an SE of size i , and n is the total number of bothats. By definition of the tophat and bothat by reconstruction, we have

$BP_0(x) = TP_0(x) = I(x)$. Given Equation 3-1 and 3-2, the tophat profile can also be defined as a granulometry made with the tophat by reconstruction, while the bothat profile can be defined as

antigranulometry made with bothat by dual reconstruction. By connecting the TP and the BP together, the MP of image I is defined as the following $2n + 1$ dimensional vector:

$$MP(x) = [BP_n(x), \dots, I(x), \dots, TP_n(x)] \quad (3-3)$$

$$MP_i(x) = \begin{cases} BP_{n-i} & \text{if } 0 \leq i < n \\ I(x) & \text{if } i = n \\ TP_i & \text{if } n < i \leq 2n \end{cases} \quad (3-4)$$

The MP for each pixel is the response of the considered pixel to tophat or bothat by reconstruction with a structuring element of increasing size. Examples of the tophat and bothat operations for a particular SE size are shown in Figure 3-1. We can see that the bothat emphasizes local minima, such as streams, whereas the tophat emphasizes local maxima, such as berms.

The derivative (difference equation actually since the MP is discrete) of the morphological profile is defined as a vector where the measure of the slope of the tophat-bothat profile is stored for every step of an increasing SE series. Specifically, the derivative of the tophat profile, $\Delta TP(x)$, is defined as the vector

$$\Delta TP_i(x) = |TP_i(x) - TP_{i-1}(x)|, \forall i \in [1, n] \quad (3-5)$$

Similarly, the derivative of the bothat profile $\Delta BP(x)$ is defined as the vector

$$\Delta BP_i(x) = |BP_i(x) - BP_{i-1}(x)|, \forall i \in [1, n] \quad (3-6)$$

We can then define the DMP as the vector

$$DMP_j(x) = \begin{cases} \Delta BP_{n-j+1}(x) & \text{if } 1 \leq j \leq n \\ \Delta TP_{j-n}(x) & \text{if } n+1 \leq j \leq 2n \end{cases} \quad (3-7)$$

where $2n$ is the total number of iterations, j is SE size. From Equation 3-7, if the high responses are near the central position of the DMP vector, there are mainly small structures in the image.

By contrast, high responses either towards the left or the right imply there are large structures in the image. These larger structures are either darker (i.e. high response in the bothat profile $\Delta BP(x)$) or lighter (i.e. high response in the tophat profile $\Delta TP(x)$) than the surroundings. Basically, the DMP provides the information about the size and type of the structure (darker or lighter) in the image by the response location in the DMP histogram.

The size and type of the structures can be determined by the distance from the center to peak response position in the profile and on which side the peak occurs in the histogram of the DMP values (see Figure 3-2). While the above mentioned approaches do not require a particular metric for the morphological transforms, the DMP approach requires the use of the tophat and bothat pair by reconstruction, using a geodesic metric.

3.3 Principal Component Analysis

The DMP is a rather high dimensional representation (Section 3.2), leading to a length $2n$ profile for every single pixel in the DEM. Principal Component Analysis (PCA) is a well known technique that can be used to reduce multidimensional data sets to lower dimensions for analysis. Depending on the field of application, it is also named the discrete Karhunen-Loève transform, the Hotelling transform or Proper Orthogonal Decomposition (POD) (Gonzalez *et al.*, 2002). PCA attempts to find the least redundant set of bases (with respect to second order statistical moments) in which to represent the data by projecting the data in the directions of maximum variance.

Let the training set of DMPs be $\Gamma_1, \Gamma_2, \Gamma_3, \dots, \Gamma_M$, where M is the number of training and $\Gamma_n, 1 \leq n \leq M$, is the DMP vector for pixel n in an image. The size of Γ_n is $L \times 1$, where L is the total number of iterations in DMP. The average DMP of the set is defined by

$$\Psi = \frac{1}{M} \sum_{n=1}^M \Gamma_n \quad (3-8)$$

Each DMP differs from the average by the vector $\Phi_i = \Gamma_i - \Psi$. The vector u_k and scalars λ_k , $1 \leq k \leq L$, are the eigenvectors and eigenvalues, respectively, of the covariance matrix,

$$C = \frac{1}{M} \sum_{n=1}^M \Phi_n \Phi_n^T \quad (3-9)$$

After sorting eigenvalues, we chose some largest eigenvectors corresponding to the eigenvalues. To classify the classes (new DMP vectors) efficiently, the proper value of k must be chosen. Since the eigenvalues are close to zero after the 13th largest eigenvalue, we chose 13 here. The new DMP Γ is transformed into its eigenvector components (projected into ‘‘DMP space’’) by a simple operation,

$$w_k = u_k^T (\Gamma - \Psi) \text{ for } k = 1, \dots, L' \quad (3-10)$$

where $1 \leq L' \leq L$.

3.4 Linear Discriminant Analysis

Linear Discriminant Analysis (LDA) optimizes the ratio of between-class variance to within-class variance in any particular data set, thereby guaranteeing optimal separability with respect to the second order statistical moments (Duda *et al.*, 2001). PCA projects data in the directions of maximum variance, however, the direction of maximum variance may not be optimal for classification. LDA projects to a space which preserves directions useful for data separability, and therefore classification. The object of LDA is to perform dimensionality reduction while preserving as much of the class discriminatory information as possible. For the C -class problem, the projection is from a L -dimensional space to a $(C-1)$ -dimensional space, and it is assumed that $L \geq C$.

In C -classes, we will seek $(C-1)$ projections, $y = [y_1, y_2, \dots, y_{c-1}]$, by means of $(C-1)$ projection vectors $w_i, 1 \leq i \leq C-1$, which can be arranged by columns into a projection matrix

$$W = [w_1 | w_2 | \dots | w_{C-1}]: y_i = w_i^T x \quad \text{and} \quad y = W^T x \quad (3-11)$$

where y is the projected vector, W is projection matrix and x is the input vector.

The generalization of the within-class scatter is

$$S_w = \sum_{i=1}^C S_i \quad (3-12)$$

where C is the total number of classes and

$$S_i = \sum_{x \in \omega_i} (x - \mu_i)(x - \mu_i)^T \quad (3-13)$$

μ_i is mean vector of class i , ω_i is the class i label

$$\mu_i = \frac{1}{N_i} \sum_{x \in \omega_i} x \quad (3-14)$$

where N_i is total number of samples from class i .

The generalization of the between-class scatter is

$$S_B = \sum_{i=1}^C N_i (\mu_i - \mu)(\mu_i - \mu)^T \quad (3-15)$$

and

$$\mu = \frac{1}{N} \sum_{\forall x} x = \frac{1}{N} \sum_{x \in \omega_i} N_i \mu_i \quad (3-16)$$

where N is total number of samples from all classes. Then $S_T = S_B + S_w$ is called the total scatter matrix.

The mean vector and scatter matrices for the projected samples are defined as

$$\tilde{\mu}_i = \frac{1}{N_i} \sum_{y \in \omega_i} y \quad (3-17)$$

$$\tilde{S}_W = \sum_{i=1}^C \sum_{y \in \omega_i} (y - \tilde{\mu}_i)(y - \tilde{\mu}_i)^T \quad (3-18)$$

$$\tilde{\mu} = \frac{1}{N} \sum_{\forall y} y \quad (3-19)$$

$$\tilde{S}_B = \sum_{i=1}^C N_i (\tilde{\mu}_i - \tilde{\mu})(\tilde{\mu}_i - \tilde{\mu})^T \quad (3-20)$$

We can re-write these using a projection matrix W :

$$\tilde{S}_W = W^T S_W W \quad (3-21)$$

$$\tilde{S}_B = W^T S_B W \quad (3-22)$$

We are looking for a projection that optimizes the ratio of between-class to within-class scatter.

Since the projection is no longer a scalar (it has $C-1$ dimensions), we then use the determinant of the scatter matrices to obtain a scalar objective function,

$$J(W) = \frac{|\tilde{S}_B|}{|\tilde{S}_W|} = \frac{|W^T S_B W|}{|W^T S_W W|} \quad (3-23)$$

We seek the optimal projection matrix W^* that maximizes this ratio. It can be shown that the optimal projection matrix W^* is the one whose columns are the eigenvectors corresponding to the largest eigenvalues of the following generalized eigenvalue problem (Duda *et al.*, 2001).

$$W^* = [w_1^* | w_2^* | \dots | w_{C-1}^*] = \arg \max \left\{ \frac{|W^T S_B W|}{|W^T S_W W|} \right\} \rightarrow (S_B - \lambda_i S_W) w_i^* = 0 \quad (3-24)$$

where λ_i represents the eigenvalues.

S_B is the sum of C matrices of rank one or less and the mean vectors are constrained by

$$\frac{1}{C} \sum_{i=1}^C \mu_i = \mu \quad (3-25)$$

Therefore, S_B will be of rank (C-1) or less. This means that only (C-1) of the eigenvalues λ_i will be non-zero. The projections with maximum class separability information are the eigenvectors corresponding to the largest eigenvalues of $S_W^{-1}S_B$.

3.5 Bayesian Classification

Bayesian classification is a simple probabilistic classification based on applying Bayes' theorem. If the given class labels are ω_j , where j ranges from 1 to the number of classes, and x is the vector of features derived from the data, we have

$$P(\omega_j | x) = \frac{p(x | \omega_j)p(\omega_j)}{p(x)} \quad (3-26)$$

where $p(x) = \sum_j p(x | \omega_j)p(\omega_j)$.

In words, we can re-write,

$$\text{posterior} = \frac{\text{likelihood} \times \text{prior}}{\text{evidence}} \quad (3-27)$$

The prior probability reflects knowledge of the relative frequency of instances of a class. The likelihood is the probability distribution that a given value occurs in a given class. The evidence is a scaling term to ensure $0 \leq P(\omega_j | x) \leq 1$. In its most basic form, we choose the class label that yields the *maximum a posteriori* (MAP) probability for a given sample. For forming a more general classifier, discriminant functions $g_i(X)$ can be specified for each class $i = 1, \dots, C$. We assign a sample X to class k if $g_k(X) > g_j(X)$ for all $k \neq j$. For a minimum error classifier, $g_i(X) = P(\omega_i | X)$. If f is a monotone increasing function, the collection

$h_j(X) = f(g_i(X)), i = 1, \dots, C$ forms an equivalent family of discriminant functions (Duda *et al.*, 2001), e.g.,

$$g_i(X) = P(\omega_i | X) = \frac{p(X | \omega_i)p(\omega_i)}{\sum_{j=1}^c p(X | \omega_j)p(\omega_j)} \quad (3-28)$$

$$g_i(X) = p(X | \omega_i)p(\omega_i) \quad (3-29)$$

$$g_i(X) = \ln p(X | \omega_i) + \ln p(\omega_i) \quad (3-30)$$

This expression is the well known log likelihood, and it can be readily evaluated if the densities $p(X | \omega_i)$ are multivariate normal, that is, if $p(X | \omega_i) \sim N(\mu_i, \Sigma_i)$, where X is a d dimensional vector, μ is the mean vector, and Σ is the $d \times d$ covariance matrix. The general multivariate normal density in d dimensions is written as

$$p(X) = \frac{1}{(2\pi)^{d/2} |\Sigma|^{1/2}} \exp \left[-\frac{1}{2} (X - \mu)' \Sigma^{-1} (X - \mu) \right] \quad (3-31)$$

In this case, we can re-write the discriminant function,

$$g_i(X) = -\frac{1}{2} (X - \mu_i)' \Sigma_i^{-1} (X - \mu_i) - \frac{d}{2} \ln 2\pi - \frac{1}{2} \ln |\Sigma_i| + \ln P(\omega_i) \quad (3-32)$$

In the general multivariate normal case, the covariance matrices are different for each category.

The only term that can be dropped from Equation 3-32 is the $-\frac{d}{2} \ln 2\pi$ term because it does not depend on the data, making the resulting discriminant functions inherently quadratic in X :

$$g_i(X) = X' W_i X + w_i' X + \omega_{i0} \quad (3-33)$$

where

$$W_i = -\frac{1}{2} \Sigma_i^{-1} \quad (3-34)$$

$$w_i = \Sigma_i^{-1} \mu_i \quad (3-35)$$

and

$$\omega_{i0} = -\frac{1}{2} \mu_i' \Sigma_i^{-1} \mu_i - \frac{1}{2} \ln |\Sigma_i| + \ln P(\omega_i) \quad (3-36)$$

3.6 Result and Discussion

To build the Morphological Profiles (MPs), it is necessary to choose a shape and a range of sizes for the Structure Element (SE). A disk shape is often used because it has the property of being independent to changes of orientation (i.e. isotropic). Here, we use a disk. The number of different SE sizes and their increments in size are to be chosen to cover all the structures of interest in the image. This is chosen in accordance with the resolution of the data and the range of possible variations in the size of the structures of interest. In the case presented here, a 21-dimensional morphological profile was created (ten bothats, ten tophats, along with the original image) using a circular morphological structuring element with an increasing radius. A 20-dimensional DMP (Differential Morphological Profile) was then generated. Thus, each pixel in the DEM gets associated with a 20-dimensional feature vector.

We employ 6 classes in the Hogtown Creek site: 1.Stream, 2. Unstructured watery areas (e.g. ponds, borrow pits, and sink holes), 3. Forest floor outside of the stream, 4.Road, 5. Suburban area that is not a road, 6.Earthen Berms (See Figure 3-3).

PCA (with 13 eigenvectors) and LDA are applied for feature extraction and reduction in the Bayesian classifier. The classification accuracies for the different feature sets were compared to accuracies achieved for the full differential morphological profile.

The test image of Hogtown Creek in this experiment is bare-surface DEM_{G3}. The imaged area is 290m×521m, with 1m×1m pixels. Approximately half of the samples were used for training and the rest for testing the approaches (See Table 3-1). We ran the experiment one

hundred times with randomly selected samples for training and found the mean and variance of detection percentages. Table 3-2 shows the experimental results.

From Table 3-2, we can see the stream is very successfully classified in all three cases. The berm class is also successfully classified. Considering the fact that the elevation ranges across most roads are considerably smaller than those across streams or berms, the road accuracies are acceptable. LDA reduces the dimensionality to, at most, $C-1$, where C is the number of classes ($C=6$). But in PCA, the dimension is changed from 1 to N dimensions (in this case, N was equal to twenty). Here, LDA uses only 5 dimensions. PCA can project up to the original dimensionality of the data (20 in this case), but the top 13 PCA channels, which have most of the variance information (about 97%), were used (i.e. the eigenvalues are close to zero after the 13th largest eigenvalue). So in this case, PCA requires more information than LDA. Often times LDA is expected to be superior to PCA because it deals directly with class discrimination. But this is not always the case. When the training data set is small, PCA can outperform LDA and, also, PCA is sometimes less sensitive to different training data sets (Martinez *et al.*, 2001). Here, PCA contains almost all of the information and the berm class has a particularly small amount of available training data, and so it is not surprising that LDA results suffer somewhat.

The detection percentages of other classes (classes 2, 3, and 5) are low because they are easily confused with each other. This is perhaps not surprising given that the classification was based on local morphology at the scale of the structuring elements. One would not necessarily expect a morphological operator that detects streams to differentiate between non-road city terrain and non-stream forested terrain. In the future, we will likely merge some of those classes

because the main intent here is to extract roads and streams from the DEM, not to classify all kinds of terrain.

In the Hatchett data, we have two classes: 1. Stream, 2. Outside Stream (forest terrain that is not a stream) (See Figure 3-4) since the other classes were not present. We applied the same procedures to Hatchett Creek as we did to Hogtown Creek. Table 3-3 shows the number of samples used for training and testing. The experimental results of Hatchett Creek can be found in Table 3-4. Streams are classified well in full DMP, PCA, and LDA. The result of LDA is slightly lower than other two approaches, likely due to the reduced dimensionality.

Red Wall Canyon in Death Valley has two classes: 1. Stream, 2. Outside Stream (See Figure 3-5). Like Hogtown Creek and Hatchett Creek, the same procedures are applied to Red Wall Canyon data and the results are shown in Table 3-6. Table 3-5 shows the number of samples used for training and testing. As it works in Hogtown Creek and Hatchett Creek, the streams are classified well in all cases.

In the Hogtown Creek and Red Wall Canyon cases, the performance difference between PCA and LDA is trivial. However, in the Hatchett case, there is a performance difference of about 5% between PCA and LDA. One possible reason is LDA does not have enough information for the separation because of total number of classes, C ($C=2$).

Red Wall Canyon outperforms than Hogtown Creek and Hatchett Creek with regards to non-stream detection performance. This may be due to the use of the vegetation filter on Hogtown Creek and Hatchett Creek. It is more difficult to perfectly remove the non-ground LiDAR points in densely vegetated forests than in sparsely vegetated areas like Red Wall Canyon.

3.7 Comparison of C* Algorithm, DMP, and D8

In the field of hydrology, the most commonly used approach to infer the locations of streams is the algorithm known as D8 (TauDEM, 2005). The name derives from the 8 neighboring pixels around the center pixel of a 3×3 sliding window. The algorithm was created to be used on the types of DEM data that have been most often used to date. These DEMs are typically generated from stereo aerial photography, such as the USGS National Elevation Dataset (USGS, 2006), or from interferometric radar, such as the NASA Shuttle Radar Topography Mission (SRTM, 2006). They generally have spatial resolutions of 30 m, but in some cases the resolutions are as fine as 10 m. Regardless of the resolution, however, these sensing modalities generally fail to explicitly image stream channels. Thus, the D8 algorithm is predicated on local gradients rather than on stream channel morphology. Rainwater is assumed to flow from a given pixel towards the neighboring pixel that offers the steepest gradient descent.

The class of stream locating algorithms to which D8 belongs is generally referred to as watershed algorithms (TauDEM, 2005). Slight variations exist in the hydrologic literature, including the D_{∞} algorithm (TauDEM, 2005), but they all work in the same general manner. While D8 works well on coarse-scale DEMs with large topographic relief, it often does not work well on flat areas with small closed watersheds, which are common in the coastal plains of the southeastern United States. Yet, these watershed algorithms are still used widely because they are considered to be the best available. With the greater availability of fine resolution (5m down to 1m) DEMs derived from airborne LiDAR, it is now possible to explicitly image stream channels and automatically detect them. The C* and DMP algorithms are able to exploit this new DEM technology and resolution and detect streams in a fundamentally different manner than the D8 class of algorithms.

We wish to compare the performance of the C* and DMP approaches for stream detection to each other and to the widely used D8 algorithm. We measured the detection performances of the C* algorithm, DMP, and D8 on simulated data, Hogtown Creek data, Hatchett Creek data, and Red Wall Canyon data. To implement the D8 algorithm, we used the TauDEM software package, which is available on the Web [<http://hydrology.neng.usu.edu/taudem/>]. The D8 flow direction grid defines a network of flow directions that extends to each grid cell (i.e. pixel) in the DEM. Then TauDEM orders the network according to the Strahler (TauDEM, 2005) ordering system. In the Strahler method, pixels that do not have any other pixels draining into them are order $S_{order} = 1$. Higher order numbers designate pixels that have increasingly higher numbers of pixels from which water would drain into them. When two (or more) flow paths of different order converge, the order of the downstream flow path is the order of the highest incoming flow path. When two (or more) flow paths of equal order converge the downstream flow path is increased by 1. This is implemented as

$$S_{order} = \max \left\{ \begin{array}{l} \text{highest input flow path order,} \\ \text{second highest input flow path order} + 1 \end{array} \right\} \quad (3-37)$$

which generalizes the common definition to cases where more than two flow paths converge at a point.

Intuitively, we can see that locations, such as stream channels, into which water that has accumulated over a large area flows, will have relatively high Strahler orders. So if one displays all of the DEM pixels with a Strahler order over a certain value, the locations of streams and ponds can be indirectly estimated. Unfortunately, there is no mechanism in the D8 algorithm to automatically determine the optimal threshold for the Strahler order. A user-specified threshold is typically chosen that yields a stream map that appears to be the most reasonable based on knowledge of the local hydrology (TauDEM, 2005). In this comparison, we thresholded the D8

result at Strahler order 5 on the simulated DEM, and at order 6 on the Hogtown Creek, Hatchett Creek and Red Wall Canyon sites to produce the best agreement with ground truth and informed visual interpretation of the DEMs.

Figure 3-6 shows results from the three algorithms on the simulated data, and Table 3-7 shows the corresponding Error Metrics. What we see in Figure 3-6 is that the D8 clearly fails to detect the stream channel in many locations. Furthermore, it erroneously detects false streams in some locations simply because of the presence of local minima in the DEM. The C* and DMP results both appear to match the true stream well. As one might expect, the multiscale nature of the DMP responds to a greater variety of channel widths than does C*, which uses a single SE size. This is evidenced by the greater number of small feeder channels that are detected in the DMP result. In Table 3-7, we see that the C* algorithm has a slightly lower value for EM4 than does DMP, but it also has a lower value for N_{TD} . This is because the small numerous feeder paths that direct water into the stream were not explicitly encoded into the simulated stream. So when the DMP detects them, many are counted as false positives (EM2). In this case, we interpret the C* algorithm as giving a slightly better performance than DMP in detecting only the main stream channel, while the DMP gives a slightly better performance than C* in detecting a wider variety of incision features.

Figure 3-7 shows analogous results to Figure 3-6 for the Hogtown site, and Table 3-8 lists the error performances. Again, the D8 has the worst overall detection result. In fact, it mistakenly “detects” part of a road running from (270 in vertical axis, 98 in horizontal axis) up to (100, 98) and another road running from (170, 180) up to (50, 180). The C* algorithm and DMP method give fairly similar results to each other. DMP still detects more true pixels (higher N_{TD}) than C*, but has slightly larger EM3 and EM4 values.

Figure 3-8 demonstrates similar results to Figure 3-6 and Figure 3-7 for the Hatchett site, and Table 3-9 shows the error performances. Once more, comparing all methods, D8 has the worst overall detection performance. The D8 erroneously detects low elevation terrain as having sufficient Strahler order to be considered “stream”. The C* algorithm and DMP methods produce similar and good results with relatively small EM4 values. DMP detects more true pixels than C*, however, it has only minimally larger EM4 values.

Finally, Figure 3-9 displays detection results for Red Wall Canyon. The D8 method does not have a lot of erroneous stream detections, as was the case in the other test sites. Table 3-10 gives the error performances for all methods. Unlike previous sites, there is not a big difference between the EM 4 values of all 3 methods. One should recall that the vegetation filter has a harder time perfectly reconstructing the bare-surface DEM in densely forested regions where only 10% - 20% of the LiDAR points typically reach the ground, as in the simulated site, Hogtown Creek, and Hatchett Creek. The input bare-surface DEM for Red Wall Canyon is therefore a better representation of the true ground surface. Based on results of Hogtown Creek, Hatchett Creek, and Red Wall Canyon, C* and DMP are found to work well for stream detection in the most challenging case of densely forested areas. All three methods, including the conventional D8 technique, produce acceptable results in non-forested areas only. The relatively wide and straight nature of the channels in Red Wall Canyon, may also play a role in the improved performance of D8. The DMP algorithm tends to pick up more incision features and small pits in the surface than the other two, which may be useful for understanding incipient channel formation.

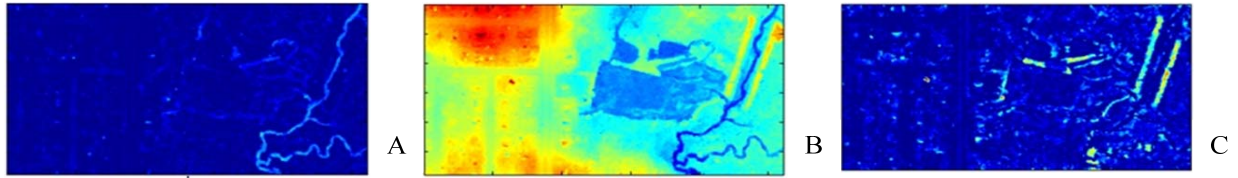


Figure 3-1. Morphological Profile for the Hogtown Creek site. The structuring elements are disks. A) Bothat profile with SE (disk radius 3). B) Original DEM generated from LiDAR ground points gridded to $1\text{ m} \times 1\text{ m}$ pixel sizes. C) Tophat profile with SE (disk radius 3). All image sizes are $290\text{ m} \times 521\text{ m}$.

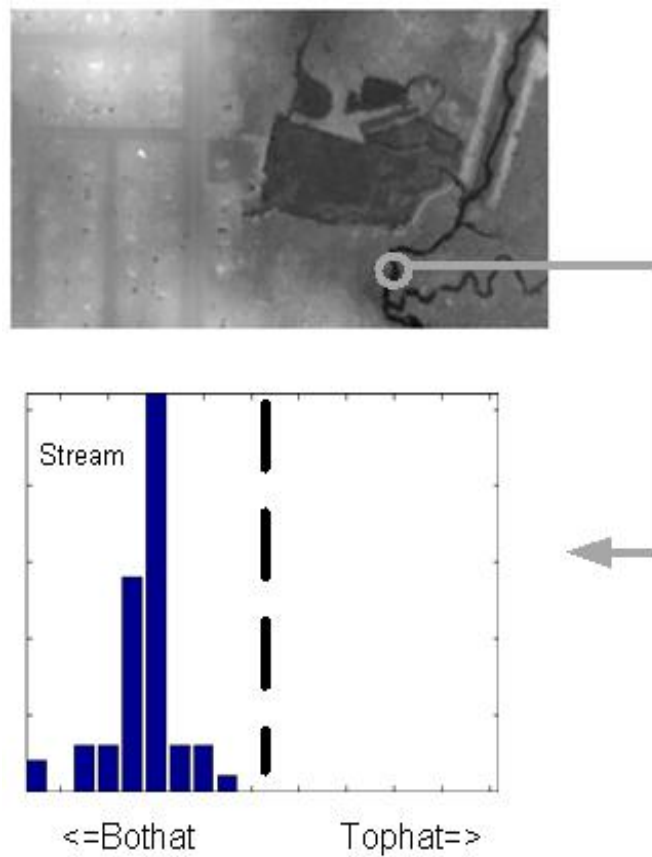


Figure 3-2. Example of a DMP for a pixel on a stream in the Hogtown DEM. A circular morphological structuring element was used with an increasing radius from 1 to 10. The peak response is on the bothat side, as one would expect for a stream.

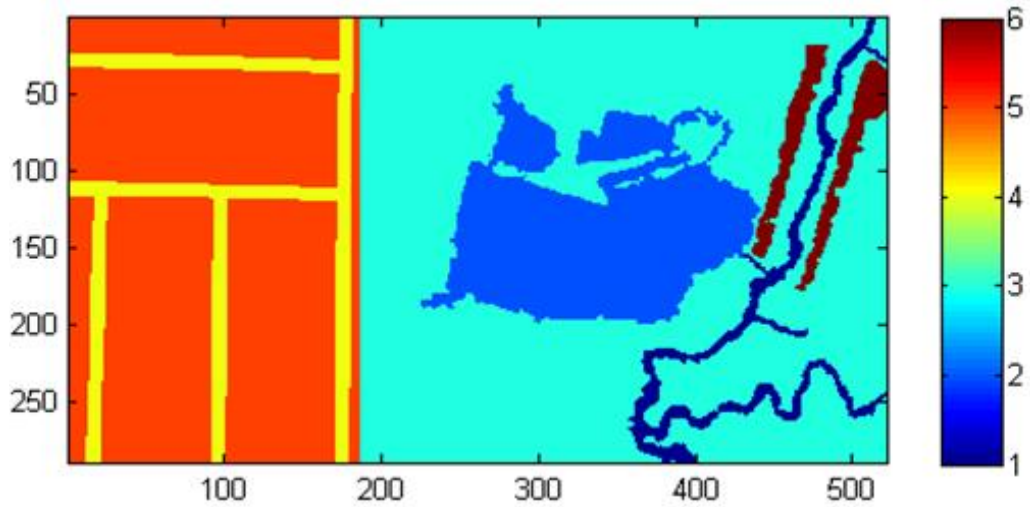


Figure 3-3. Ground truth over the Hogtown site based on image interpretation and repeated field surveys: 1.Stream, 2.Unstructured watery area (borrow pit), 3.Forest floor outside of the stream, 4.Road, 5.Suburban area that is not a road, 6. Earthen berm created for flood control.

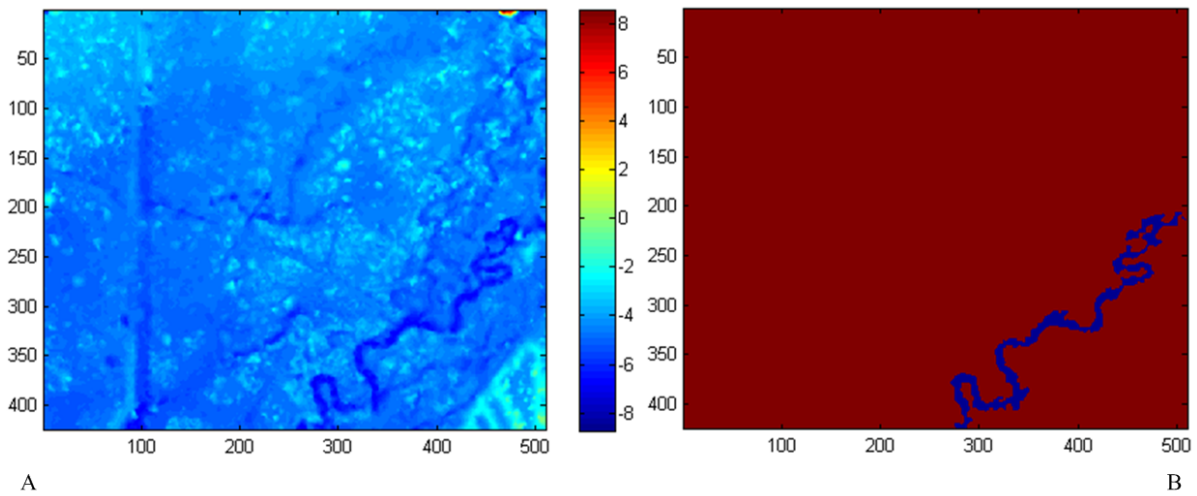


Figure 3-4. A) Bare-surface DEM of Hatchett Creek. The imaged area is 425m×510m, with 1m×1m pixels. Elevations are in meters. B) A two-class ground truth of Hatchett: Stream (blue), Outside Stream (red).

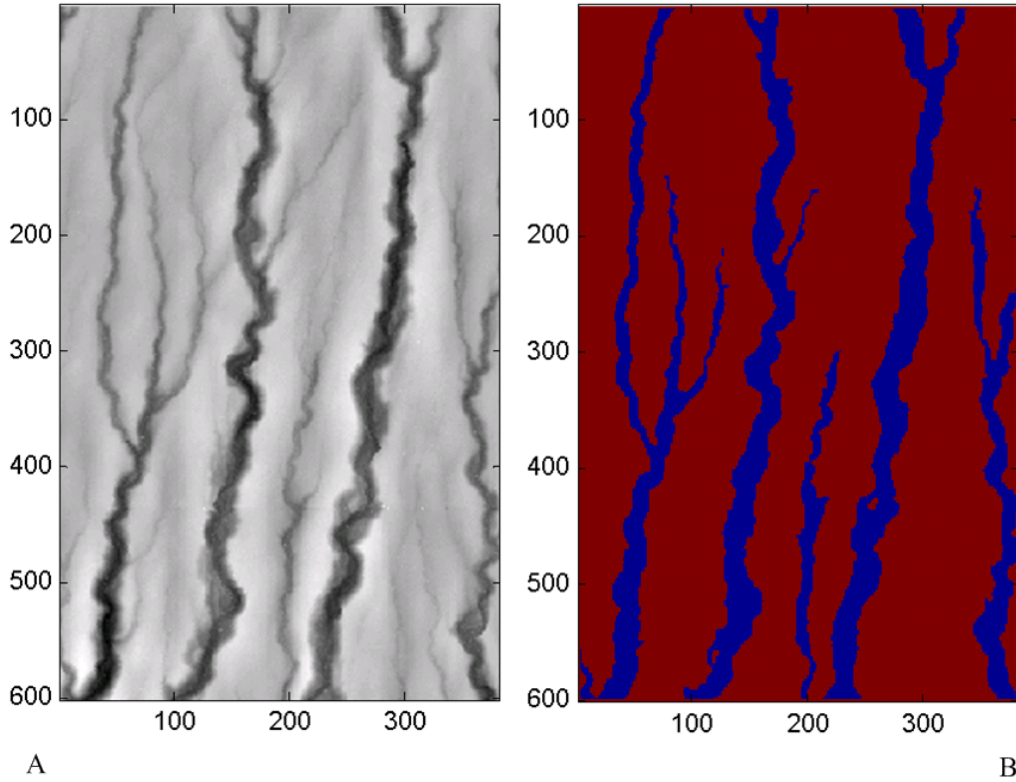


Figure 3-5. A) Bare-surface DEM of Red Wall Canyon. The imaged area is 601m×382m, with 1m×1m pixels. Elevations are in meters. B) Ground truth of Red Wall Canyon: Stream (blue), Outside Stream (red)

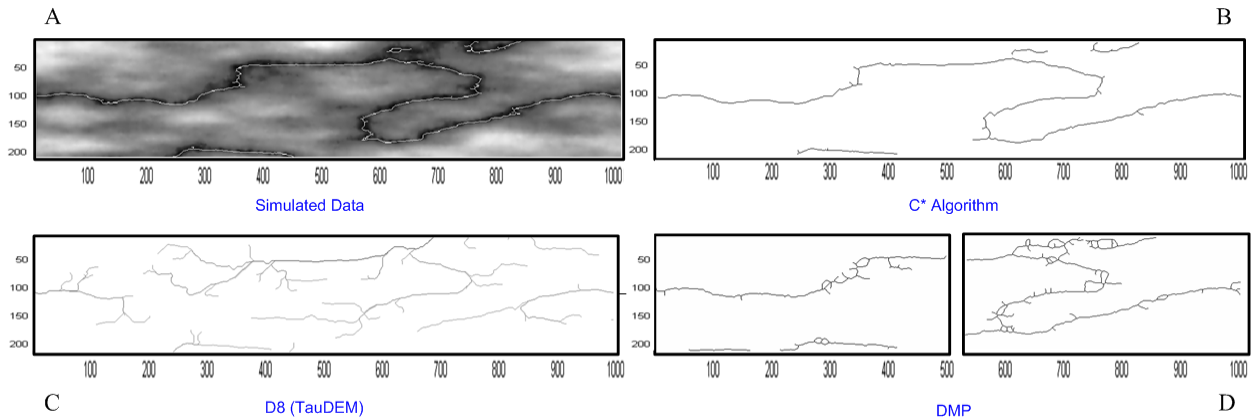


Figure 3-6. Detection results on simulated data. The DEM is 200m × 1000m, with an elevation range of 4m. The DMP result is shown in two blocks because it requires training. The left DMP block was used for training when the right DMP block is the test block and vice versa. In “A”, the white line is the “true and main” stream in the Simulated Data. It does not include the small incipient incision features that we see picked up by the algorithms.

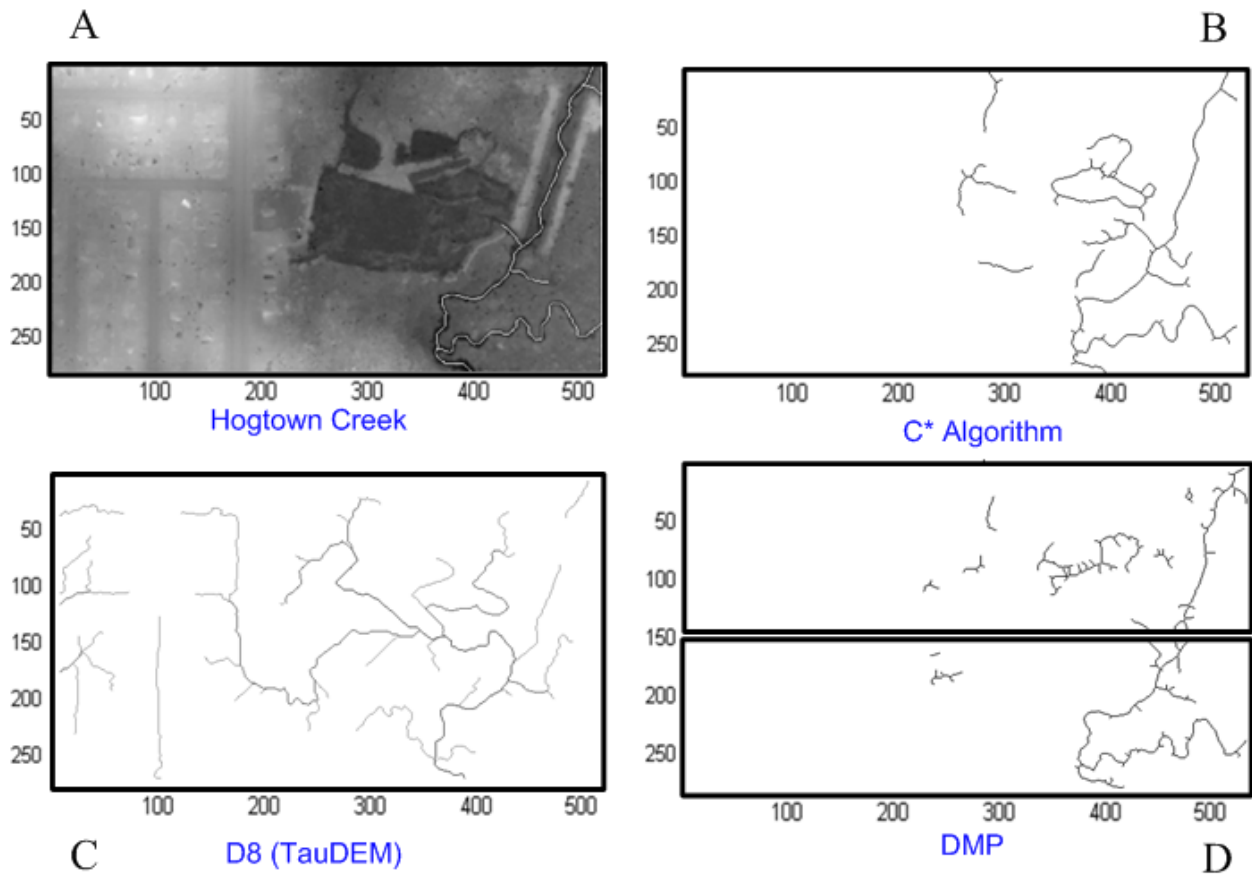


Figure 3-7. Detection results on Hogtown Creek. The DEM is 290m \times 521m, with an elevation range of 7 m. Similar to Figure 3-6, the top DMP block was used for training when the bottom DMP block is the test block and vice versa. White line in "A" is the "true and main" stream in the Hogtown Creek derived from close visual inspection of the DEM and trips to the field site. It does not include the small convergent incipient incision features that we see picked up by the algorithms.

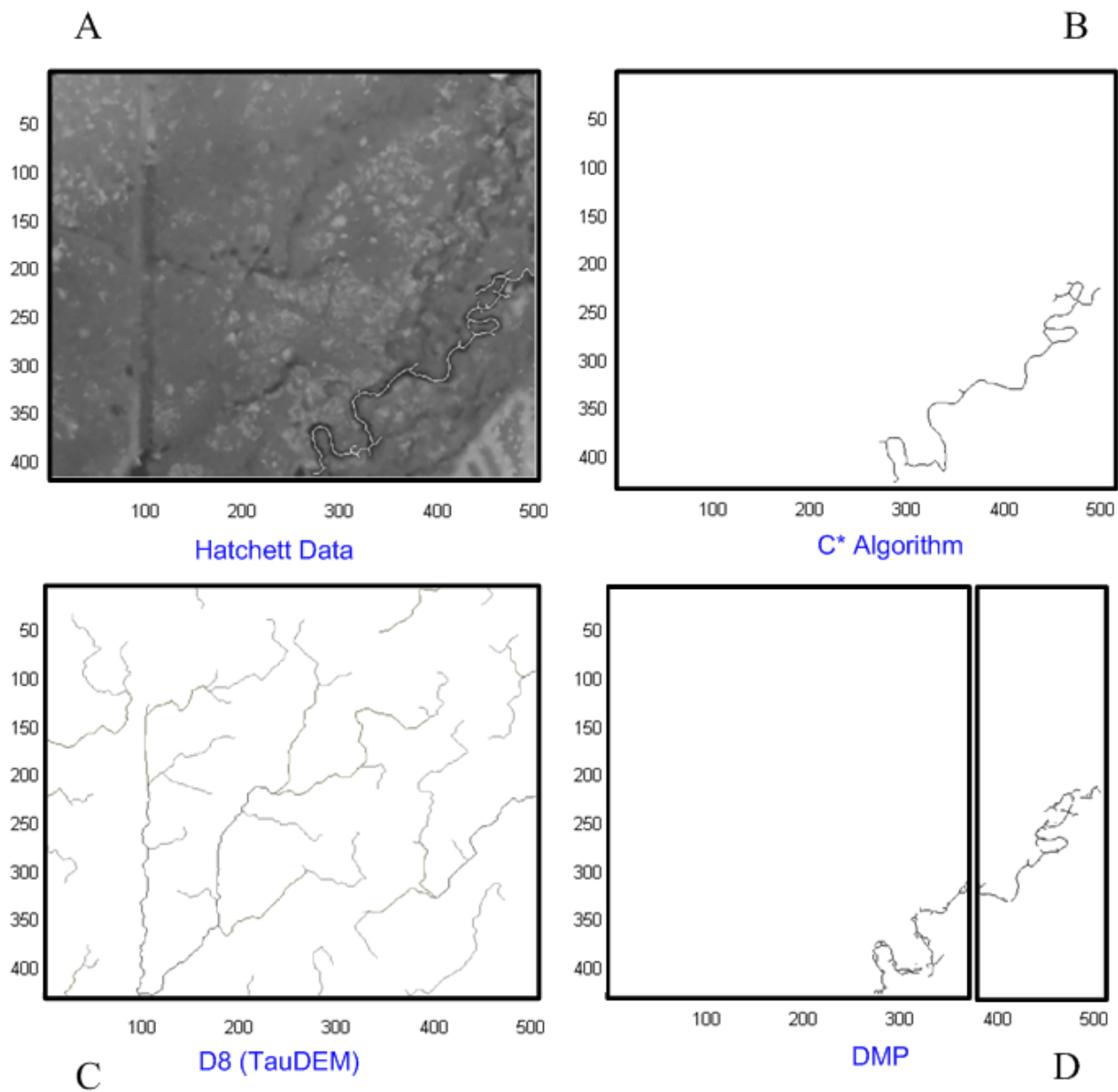


Figure 3-8. Detection results on Hatchett Creek. The DEM is $510\text{m} \times 425\text{m}$, with an elevation range of 7 m. Similar to Figure 3-6 and Figure 3-7, the left DMP block was used for training when the right DMP block is the test block and vice versa. White line is the “true and main” stream in the Hatchett Creek.

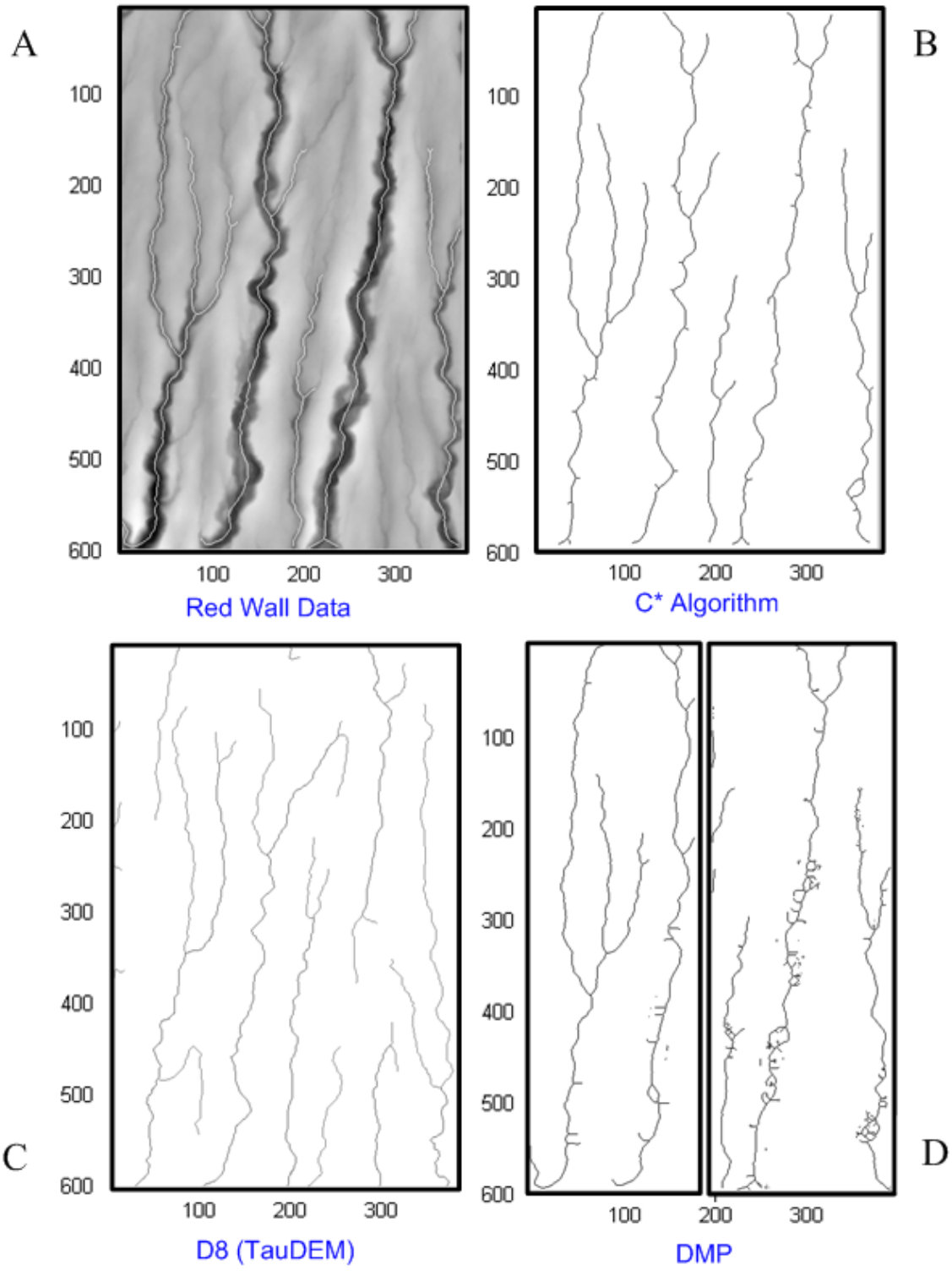


Figure 3-9. Detection results on Red Wall Canyon. The DEM is 601m \times 382 m, with an elevation range of 90m. Similar to Figure 3-6, Figure 3-7 and Figure 3-8, the left DMP block was used for training when the right DMP block is the test block and vice versa. The white line in "A" is the "true and main" stream in the Red Wall Canyon.

Table 3-1. Information classes, training, and test samples for Hogtown Creek site

Class No.	Information Class	Number of Training Samples	Number of Test Samples
1	Stream	2101	2100
2	Watery Area	9497	9496
3	Outside Stream	35375	35375
4	Road	4415	4414
5	Outside Road	22556	22555
6	Earthen Berm	1063	1063

Table 3-2. Test accuracies in percentages with variances for Hogtown Creek site

Class No.	Information Class	Full DMP (%)	PCA (%)	LDA (%)
1	Stream	94.17 (1.19)	93.75 (0.14)	92.91 (0.21)
2	Watery Area	28.74 (0.32)	23.92 (0.12)	26.00 (0.18)
3	Outside Stream	13.80 (1.13)	16.24 (0.09)	15.56 (0.06)
4	Road	89.82 (0.26)	89.18 (0.18)	86.22 (0.37)
5	Outside Road	36.30 (0.39)	37.54 (0.08)	36.64 (0.14)
6	Earthen Berm	88.14 (1.26)	86.92 (0.52)	80.38 (0.93)

Table 3-3. Information classes, training, and test samples for Hatchett Creek

Class No.	Information Class	Number of Training Samples	Number of Test Samples
1	Stream	2240	2239
2	Outside Stream	106136	105135

Table 3-4. Test accuracies in percentage with variances for Hatchett Creek

Class No.	Information Class	Full DMP (%)	PCA (%)	LDA (%)
1	Stream	90.30 (0.47)	89.70 (0.43)	84.47 (0.49)
2	Outside Stream	81.28 (0.31)	83.76 (0.14)	91.67 (0.01)

Table 3-5. Information classes, training, and test samples for Red Wall Canyon

Class No.	Information Class	Number of Training Samples	Number of Test Samples
1	Stream	22820	22820
2	Outside Stream	91971	91971

Table 3-6. Test accuracies in percentage with variances for Red Wall Canyon

Class No.	Information Class	Full DMP (%)	PCA (%)	LDA (%)
1	Stream	92.60 (0.02)	92.39 (0.02)	90.07 (0.03)
2	Outside Stream	93.53 (0.01)	93.69(0.008)	95.83(0.005)

Table 3-7. Error metrics vs. all methods on simulation

	EM 1	EM2	EM3	EM4	N_{TD}
C* Algorithm	581	22	1.6713	1.9626	1406
D8(TauDEM)	856	1741	1.9677	3.2223	1317
DMP	510	772	2.1621	2.7814	1756

N_{TD} : Number of true detected pixels

Table 3-8. Error metrics vs. all methods on Hogtown Creek

	EM 1	EM2	EM3	EM4	N_{TD}
C* Algorithm	78	740	1.3179	2.5861	315
D8 (TauDEM)	281	2187	1.2615	5.0878	201
DMP	83	558	1.7498	2.7436	485

N_{TD} : Number of true detected pixels

Table 3-9. Error metrics vs. all methods on Hatchett Creek

	EM 1	EM2	EM3	EM4	N_{TD}
C* Algorithm	135	8	1.4332	1.6642	249
D8(TauDEM)	365	3212	2.3664	8.1451	297
DMP	69	6	1.7132	1.8344	382

N_{TD} : Number of true detected pixels

Table 3-10. Error metrics vs. all methods on Red Wall Canyon

	EM 1	EM2	EM3	EM4	N_{TD}
C* Algorithm	609	128	1.7856	2.008	1975
D8(TauDEM)	1018	1239	1.7658	2.4474	1924
DMP	144	360	2.2686	2.4208	1184

N_{TD} : Number of true detected pixels

CHAPTER 4 CONCLUSIONS AND FUTURE WORK

To date, the ability to accurately detect and parameterize small streams, such as those examined here, in forested terrain has been problematic. *In situ* methods are extremely labor intensive, thus limiting their spatial density and coverage. High-resolution remote sensing methods offer the potential to characterize watersheds much more efficiently than direct field sampling. However, traditional remote sensing technologies, such as passive optical and radar, are not able to extract the necessary 3D information on surfaces below forest canopies at the required spatial resolutions to reveal streams. While modern ALSM (Airborne Laser Swath Mapping) technology offers the possibility of detecting such stream channels in forests, a method is still needed to systematically extract stream channels and estimate their characteristics.

In this work, a set of morphological operations are specified that perform this detection, demonstrating for the first time the robust extraction of small channels in low topographic relief dense forest canopies. The C* algorithm discussed and demonstrated here allows us to “mine” ALSM-derived DEMs for these important hydrologic features in a systematic way. From C*, we can extract Radius of Curvature (ROC), bank slope asymmetry, width and depth so that we determine both the planform paths of the channels as well as their 3D forms. This is valuable information for hydrologists or researchers who are studying stream channels. Of particular interest is the discovery of small features that appear to reveal incipient incision on floodplains. The detection of such features will likely prove very useful for studies of where and how channels initiate in forested watersheds.

In a second approach, we used the Differential Morphological Profile (DMP) method to determine the optimal size of the structuring element for channel detection. Additionally, we found that the morphological transformations used to build a DMP could be used as a feature set

for Bayesian classification of both channels and roads. This is critically important in urban watersheds where the stream network can be crisscrossed with numerous roads. Knowing where the roads are enables us to separate earthen dams (where the water does not pass) in the DEM from small bridges (where the water can pass). Additionally, we explored ways to reduce the dimensionality of the DMPs. The considered approaches were Principal Component Analysis (PCA) and Linear Discriminant Analysis (LDA). The use of the differential profiles in classification proved valuable, and good overall accuracies of stream detection were achieved, while the detection of roads and earthen berms also shows promise in the Hogtown Creek data. This reduction in dimensionality is motivated by the desire to run this type of stream detection on larger areas. We can also apply the DMP method to detect streams with different widths because it is a multi-scale approach.

Of primary importance is to more fully understand the performance of C* and DMP under different conditions, such as location, data density, and training, so that clear conclusions can be drawn as to their relative merits and when to use C* versus when to use DMP. Experiments should be run in the future on simulated and real data to accomplish this.

The C* and DMP algorithms are compared with a conventional algorithm (i.e. D8). Unlike our algorithms, D8 requires a user-specified threshold to obtain a result, and is quite sensitive to the choice of threshold. We used user-thresholds too in C* (e.g. when it connects segments, etc.). The main difference is that those thresholds are only on intermediate calculations and small changes in them probably don't dramatically change the final stream detection. In contrast, the threshold in D8 is on the final stream detection and has a huge impact on the D8 results. Also, it doesn't seem to have a clear relation to the physical sizes of the streams as our C* thresholds do. The C* and DMP have good performance for stream channel

detection especially in forested areas, while the conventional technique, D8, yields acceptable results in non-forested areas only.

In our Hogtown Creek classification experiment, we initially used six classes: 1. Stream, 2. Watery Area, 3. Outside Stream, 4. Road, 5. Outside Road, 6. Earthen Berm. The features of three of those classes (2: Watery Area, 3: Outside Stream, and 5: Outside Road) are not well suited for the small-scale morphology approach we use to detect streams and roads. Furthermore, detecting those classes are not central to our topic here, so one may wish change the taxonomy in future classifications so that it focuses more on detecting roads and streams from the “background” and worries less about classifying that background. In addition, a different approach altogether could be used to classify the remaining terrain once streams and roads are classified by C* or DMP. To reduce the dimensionality of DMP, we examined two well known feature extraction methods, PCA and LDA. While these did produce good stream detection results, the impact of using more or fewer components in PCA on the eventual accuracy should be explored more for different types of terrain. We may also look at more modern feature extraction methods in the future. Finally, we plan to investigate the classifier’s sensitivity to the amount and distribution of training data through more extensive areas and randomized re-sampling methods.

With the detected streams fully connected, we can begin to characterize the actual stream network rather than just the location, form of local stream channels and simple features. We could then extract network features, such as total volume, ratio of streams of different orders, the evolution of cross-section width and depth with stream order, number and spacing of convergent points (two streams becoming one), etc as one moves downstream. The systematic extraction of these features from LiDAR DEMs would be very important for hydrologists.

LIST OF REFERENCES

- Asselen, S. V., and Seijmonsbergen, A.C., 2006, Expert-driven semi-automated geomorphological mapping for a mountainous area using a laser DTM. *Geomorphology*, **78**, pp. 309-320.
- Beucher, S., and Lantuejoul, C., 1979, Use of watersheds in contour detection, *International workshop on image processing, real-time edge and motion detection*.
- Bianchin, A. and Pesaresi, M., 1994, Outils de morphologie mathématique appliqué aux images satellite pour l'analyse de l'urbanization diffuse. In *Processing EGIS-MARI 94 Conference*, Paris, France, March 29–April 1, pp. 2085-2094.
- Bowen, Z. H. and Waltermire, R. G., 2002, Evaluation of light detection and ranging (LiDAR) for measuring river corridor topography. *Journal of The American Water Resources Association*, **38**, pp. 33-41.
- Carr, M.H., 1979, Formation of Martian flood features by release of water from confined aquifers, *J. Geophys. Res.*, **84**, 2995-3007
- Cavalli, M., Tarolli, P., Marchi, L. and Fontana, G. D., 2007, The effectiveness of airborne LiDAR data in the recognition of channel-bed morphology. *Catena*, **73**, pp. 249-260.
- Chow, V. T., 1988, *Open-Channel Hydraulics* (New York: McGraw-Hill)
- Crespo, J., Serra, J. and Schafer, R., 1995, Theoretical aspects of morphological filters by reconstruction. *Signal Processing*, **47**, pp. 201-225.
- Dalrymple, T., and Benson, M.A., 1967, Measurement of peak discharge by the slope-area method. Techniques of Water-Resources Investigations Report, Chapter A2. US Government Printing Office.
- Dillabaugh, C.R., Niemann, K. O., and Richardson, D.E., 2002, Semi-automatic extraction of rivers from digital imagery, *GeoInfomatica*, **6**, pp. 263-284
- Dooge, J. C. I., 1992, *Channel Wall Resistance: Centennial of Manning's Formula*, edited by B. C. Yen (Littleton, Colorado: Water Resources Publications).
- Douglas, D.H., 1986, Experiments to locate ridges and channels to create a new type of digital elevation model. *Cartographica*, **23**, pp. 29-61
- Duda, O. R., Hart, P.E., and Stork, D.G., 2001, *Pattern Classification, 2nd ed* (New York: A Wiley-Interscience Publication)
- Fischler, M.A., Tenenbaum, J.M. and Wolf, H.C., 1981, Detection of roads and linear structures in low-resolution aerial imagery using a multisource knowledge integration technique. *Computer Graphics and Image Processing*, **15**, pp. 201-223.

- Gauckler, P., 1867, Etudes Théoriques et Pratiques sur l'Écoulement et le Mouvement des Eaux, Comptes Rendues de l'Académie des Sciences, Paris, France, **Tome 64**, pp. 818-822
- Gioia G. and Bombardelli F. A., 2002, Scaling and Similarity in Rough Channel Flows, *PHYSICAL REVIEW LETTERS*, **88**, 014501.
- Gonzalez, R. C. and Woods, R.E., 2002, *Digital Image Processing, 2nd ed* (New Jersey: Prentice-Hall)
- Goutsias, J., Vincent, L., and Bloomberg, D. S., 2000, *Mathematical Morphology and Its Applications to Image and Signal Processing* (Kluwer: Academic Publishers)
- James, L. A., Watson, D. G., and Hansen, W. F., 2007, Using LiDAR data to map gullies and headwater streams under forest canopy: South Carolina, USA. *Catena*, **71**, pp. 132-144.
- Japan Industry Technology Center, 1993, *Introduction of Computer Image Processing (Korean version)* (Seoul: Mechanics Research Press).
- Jenson, S.K. and Domingue, J.O., 1988, Extracting topographic structure from digital elevation data for geographic information system analysis, *Photogrammetric Engineering and Remote Sensing* , **54(11)**, 1593-1600.
- Johnston, E.G. and Rosenfeld, A., 1975, Digital detection of pits, peaks, ridges and ravines. *IEEE Transactions on Systems, Man and Cybernetics*, **5**, pp. 472-480.
- Jones, A. F., Brewer, P. A., Johnstone, E. and Macklin, M. G., 2007, High-resolution interpretative geomorphological mapping of river valley environments using airborne LiDAR data. *Earth Surface Processes and Landforms*, **32**, pp. 1574-1592.
- Kampa, K. and Slatton, K. C., 2004, An adaptive multiscale filter for segmenting vegetation in ALSM data. In *Proceeding IEEE 2004 International Geoscience and Remote Sensing Symposium (IGARSS)*, 20-24 September, **6**, pp. 3837-3840.
- Knighton, D., 1998, *Fluvial Forms and Processes: A New Perspective* (Arnold Press).
- Laliberte, A.S., Johnson, D.E., Harris, N.R., and Casady, G.M., 2001, Stream change analysis using remote sensing and Geographic Information Systems (GIS). *Journal of Range Management*, **54**: pp. 22-50.
- Lashermes, B., Georgiou, E. F. and Dietrich, W. E., 2007, Channel network extraction from high resolution topography using wavelets. *Geophysical Research Letters*, **34**, L23S04.
- Leopold, L. B., Wolman, M. G. and Miller, J. P., 1964, *Fluvial Processes in Geomorphology* (San Francisco: W. H. Freeman and Co.)
- Lindsay, J. B., 2006, Sensitivity of channel mapping techniques to uncertainty in digital elevation data. *International Journal of Geographical Information Science*, **20**, pp. 669-692.

- Martinez, A. M. and Kak, A. C., 2001, PCA versus LDA. *IEEE Transactions on Pattern Analysis and Machine Intelligence*, **23**, pp. 228-233.
- Mason, D. C., Scott, T. R. and Wang, H. J., 2006, Extraction of tidal channel networks from airborne scanning laser altimetry. *ISPRS Journal of Photogrammetry & Remote Sensing*, **61**, pp. 67-83.
- Montgomery, D.R. and Foufoula-Georgiou, E., 1993, Channel network source representation using digital elevation models. *Water Resources Research*, **29**, pp. 3925-3934.
- O'Callaghan, J.F. and Mark, D.M., 1984, The extraction of drainage networks from digital elevation data. *Computer Vision, Graphics, & Image Processing*, **28**, pp. 323-344.
- Otsu, N., 1979, A threshold selection method from gray-level histograms. *IEEE Transactions on Systems, Man, and Cybernetics*, **9**, pp. 62-66.
- Pesaresi, M., 1993, *Analisi Numerica dello spazio edificato nella città diffusa* (Venice, Italy: Technical Report. IUAV DAEST)
- Pesaresi, M. and Benediktsson, J. A., 2001, A new approach for the morphological segmentation of high-resolution satellite imagery. *IEEE Transactions on Geoscience Remote Sensing*, **39**, pp. 309-320.
- Pesaresi, M. and Kannelopoulos, I., 1999, Detection of urban features using morphological based segmentation and very high resolution remotely sensed data. *Machine Vision and Advanced Image Processing in Remote Sensing*, Kannelopoulos, I., Wilkinson, G. G. and Moons, T., Eds. (Berlin, Germany: Springer-Verlag).
- Peucker, T.K. and Douglas, D.H., 1975, Detection of surface-specific points by local parallel processing of discrete terrain elevation data. *Computer Graphics and Image Processing*, **4**, pp. 375-387.
- Shrestha, R., Carter, W., Slatton, K.C., Dietrich, W., 2007, 'Research-Quality' Airborne Laser Swath Mapping: The Defining Factors, ver. 1.1. *National Center for Airborne Laser Mapping (NCALM)*, <http://www.ncalm.ufl.edu/>, (accessed 22 June 2007).
- Soille, P. and Pesaresi, M., 2002, Advances in mathematical morphology applied to geosciences and remote sensing. *IEEE Transactions on Geoscience Remote Sensing*, **40**, pp. 2042-2055
- Soille, P., 2003, *Morphological Image Analysis—Principles and Applications*, 2nd ed. (Berlin, Germany: Springer-Verlag).
- NASA Shuttle Radar Topography Mission (SRTM), 2006, URL: <http://www2.jpl.nasa.gov/srtm/> (accessed 05 June 2008)
- Terrain Analysis Using Digital Elevation Models (TauDEM), 2005, URL: <http://hydrology.neng.usu.edu/taudem/> (accessed 05 June 2008)

USGS National Elevation Dataset, 2006, URL <http://ned.usgs.gov/> (accessed 05 June 2008)

BIOGRAPHICAL SKETCH

Hyun-chong Cho was born in Suwon, South Korea. He received his B.S. and M.S. degrees in electrical and electronic engineering from Gyeongsang National University, South Korea in 1999 and 2001 respectively. From 1997 to 1998, he was an exchange student with a full scholarship in information and electronic engineering from Nagoya University, Japan. Since 2002, he has been working toward his Ph.D. degree in electrical and computer engineering at the University of Florida, Gainesville. He began working under the supervision of Dr. K. Clint Slatton in 2005. His research interests include remote sensing, image processing, and adaptive signal processing, especially related to airborne laser swath mapping (ALSM) applications.